Monthly Notices
of the
ROYAL ASTRONOMICAL SOCIETY

Mon. Not. R. Astron. Soc. **427,** 1363–1383 (2012) doi:10.1111/j.1365-2966.2012.22024.x

Multipole fine structure of the cosmic microwave background: reconstruction of the temperature power spectrum

Roman Tomaschitz★

Department of Physics, Hiroshima University, 1-3-1 Kagami-yama, Higashi-Hiroshima 739-8526, Japan

Accepted 2012 August 31. Received 2012 August 27; in original form 2012 July 3

ABSTRACT

The fine structure of the temperature power spectrum of the cosmic microwave background (CMB) radiation is investigated in the presently accessible multipole range up to $l \sim 10^4$. The temperature fluctuations are reproduced by an isotropic Gaussian random field on the unit sphere, whose Green function is defined by a Hermitian matrix kernel inferred from the data sets by way of spectral fits. The reconstruction of the temperature autocorrelation function from the measured multipole moments C_l is a classical inverse problem, which does not require specification of cosmic evolution equations for the photon density. The scale-invariant correlation function admits a multipole expansion in zonal spherical harmonics. The multipole coefficients are obtained as averages over Hermitian spectral matrices determining the angular power spectrum of the spherical random field. The low-l multipole regime of the CMB temperature fluctuations is composed of overlapping Gaussian peaks, followed by an intermediate oscillatory regime manifested by a modulated exponentially decaying C_l slope. The high-l regime above $l \sim 4000$ comprises a power-law ascent with exponential cut-off. The fine structure of the Gaussian, oscillatory and high-l regimes is reproduced by zooming into the respective l intervals on linear and logarithmic scales.

Key words: cosmic background radiation – cosmology: theory.

1 INTRODUCTION

The goal is the reconstruction of the temperature multipole spectrum of the cosmic microwave background (CMB) from the measured data sets. There are now quite precise measurements available, stretching over a multipole range of up to $l \sim 10^4$ (Jones et al. 2006; Brown et al. 2009; Reichardt et al. 2009, 2012; Sievers et al. 2009; Nakamura et al. 2010; Das et al. 2011; Jarosik et al. 2011; Keisler et al. 2011; Larson et al. 2011). This makes it worthwhile to have a closer look at the multipole fine structure of the temperature autocorrelation function throughout this range, by zooming into subintervals, and to figure out ways of modelling it. We will find an isotropic Gaussian random field on the unit sphere with an analytically tractable Green function capable of reproducing the observed fine structure of the CMB temperature power spectrum over the complete multipole range accessible today.

In Section 2, we sketch the general setting, the Planckian photon distribution with a fluctuating temperature variable treated as spherical Gaussian random field. We develop the formalism of random fields on the two-sphere to the extent needed to model fluctuating CMB power spectra. We study spherical Green functions with Hermitian matrix kernels, and perform the multipole expansion thereof. In Appendix A, we sketch orthogonality and completeness relations of Legendre expansions in zonal spherical harmonics, appropriate for isotropic scalar random fields. The Gaussian random field is completely determined by specifying the positive-definite Hermitian kernel of the two-point correlation function, which can be inferred from a multipole spectral fit.

This approach to CMB fluctuations deviates from Green function techniques traditionally used in field theory, which are based on evolution equations derived from a Hamiltonian or Lagrangian. Here, we reconstruct the spectral kernel of the spherical Gaussian random field from a fit of the temperature power spectrum, now available in good accuracy over an extended multipole range. Spectral fits of multipole moments C_l are usually presented on compressed linear or logarithmic multipole scales, which tend to conceal the fine structure of the data sets. Here, we employ an analytic method based on Hermitian spectral matrices, which is quite explicit and capable of reproducing the fine structure of the $\langle TT\rangle$ autocorrelation in the resolution observable today. This reconstruction of the Green function of the spherical random

★E-mail: tom@geminga.org

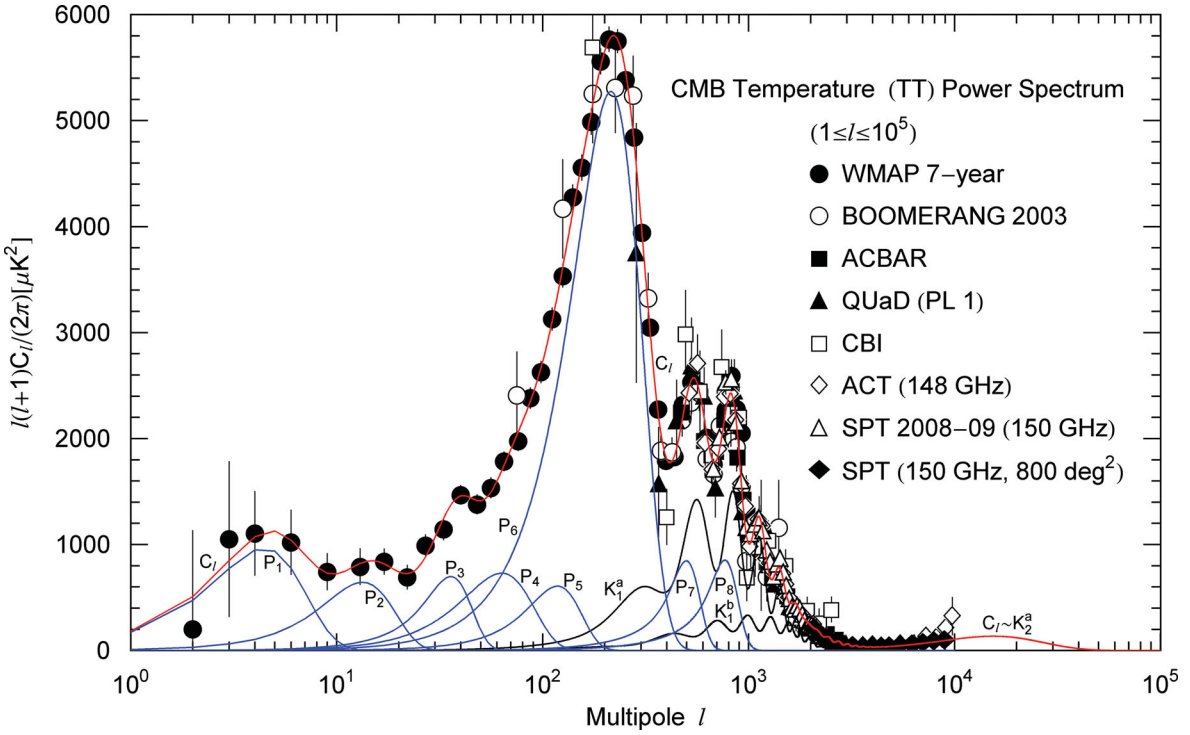

Figure 1. CMB temperature power spectrum covering the multipole range $1 \le l \le 10^5$. Data points are from 7-year *Wilkinson Microwave Anisotropy Probe* (*WMAP*, Jarosik et al. 2011; Larson et al. 2011), BOOMERANG (Jones et al. 2006), Arcminute Cosmology Bolometer Array Receiver (ACBAR, Reichardt et al. 2009), QUaD (pipeline 1) (Brown et al. 2009), Cosmic Background Imager (CBI, Sievers et al. 2009), Atacama Cosmology Telescope (ACT, at 148 GHz; Das et al. 2011), South Pole Telescope (SPT) 2008–2009 (at 150 GHz; Keisler et al. 2011) and SPT (at 150 GHz, covering 800 deg^2; Reichardt et al. 2012). In Figs 2–13, we study this multipole spectrum by zooming into various l intervals on linear and logarithmic scales, obtaining close-ups of this figure that reveal the fine structure of the multipole moments C_l and illustrate the quality of the fit ranging over four decades in l. The peak in the fifth decade is an extrapolation based on SPT data points. The moments C_l are obtained by adding the Gaussian peaks $P_{i=1,\dots,8}$, the oscillatory multipole components labelled K_1^a and K_1^b, and the extended non-Gaussian high-l peak K_2^a at $l \sim 15\,400$. The low-l region consists of Gaussian peaks, with crossover into the oscillatory regime in the third decade. The fit C_l is drawn as polygon with vertices at integer multipole index l.

field from the actual data sets is particularly attractive with regard to CMB power fluctuations, as it does not require specification of cosmic interaction mechanisms of the photon density.

In Section 3 and Appendix B, we study the Hermitian spectral matrices in the integral kernels of the multipole coefficients. We use an Euler-type representation assembled from SU(N) subgroups and diagonal matrices with Gaussian power-law densities defining the spectral amplitudes. As for CMB correlations, it suffices to consider two-dimensional unitary groups, which generate the modulations seen in the intermediate multipole range.

In Section 4, we derive scaling relations for the multipole coefficients C_l of the spherical random field; the CMB temperature power fits are performed in the scale-invariant limit. The multipole coefficients are obtained by averaging products of spherical Bessel functions and derivatives thereof with Hermitian spectral matrices. In the scale-invariant CMB fits, all Bessel derivatives drop out, so that the spectral average only involves squares of spherical Bessel functions.

In Section 5, we perform the multipole fit of the CMB temperature fluctuations. Figs 1–5 give an overview: the spectral map in Fig. 1 covers the complete multipole range investigated ($1 \le l \le 10^5$). The low-l region comprises a precursory Gaussian regime composed of merged peaks of roughly equal height, followed by a main peak, which is likewise Gaussian, cf. Fig. 2. This is followed by a transitional regime of two non-Gaussian peaks, terminating in an oscillatory descending slope, cf. Fig. 3. The high-l regime consists of a slowly rising power-law slope, cf. Fig. 4, terminating in exponential decay, and producing a peak at about $l \sim 15\,400$, cf. Fig. 5. The quality of the depicted data sets allows us to zoom into the enumerated multipole regimes and to reconstruct the C_l fine structure, cf. Figs 6–13. In Section 6, we sketch multicomponent spherical random fields, and discuss cosmic variance in the context of this reconstruction. In Section 7, we present our conclusions.

2 CMB TEMPERATURE FLUCTUATIONS: GENERAL SETTING

We study angular fluctuations of the temperature in the Planckian photon distribution, $f(\boldsymbol{p}) = 1/[\mathrm{e}^{p/(k_\mathrm{B}T_\mathrm{b}(\boldsymbol{p}_0))} - 1]$, where k_B is the Boltzmann constant, and we have put $\hbar = c = 1$. The angular dependent background temperature is denoted by $T_\mathrm{b}(\boldsymbol{p}_0)$, where the angular variable $\boldsymbol{p}_0$ is the unit vector of the photon momentum $\boldsymbol{p} = p\boldsymbol{p}_0$. It is convenient to factorize the temperature field as $T_\mathrm{b}(\boldsymbol{p}_0) = T_0(1 + \delta T_\mathrm{b}/T_0)$, where $T_0 \approx 2.7$ K is the present-day mean background temperature and $\delta T_\mathrm{b} = T_\mathrm{b}(\boldsymbol{p}_0) - T_0$ is the fluctuating field with zero mean. We conformally rescale

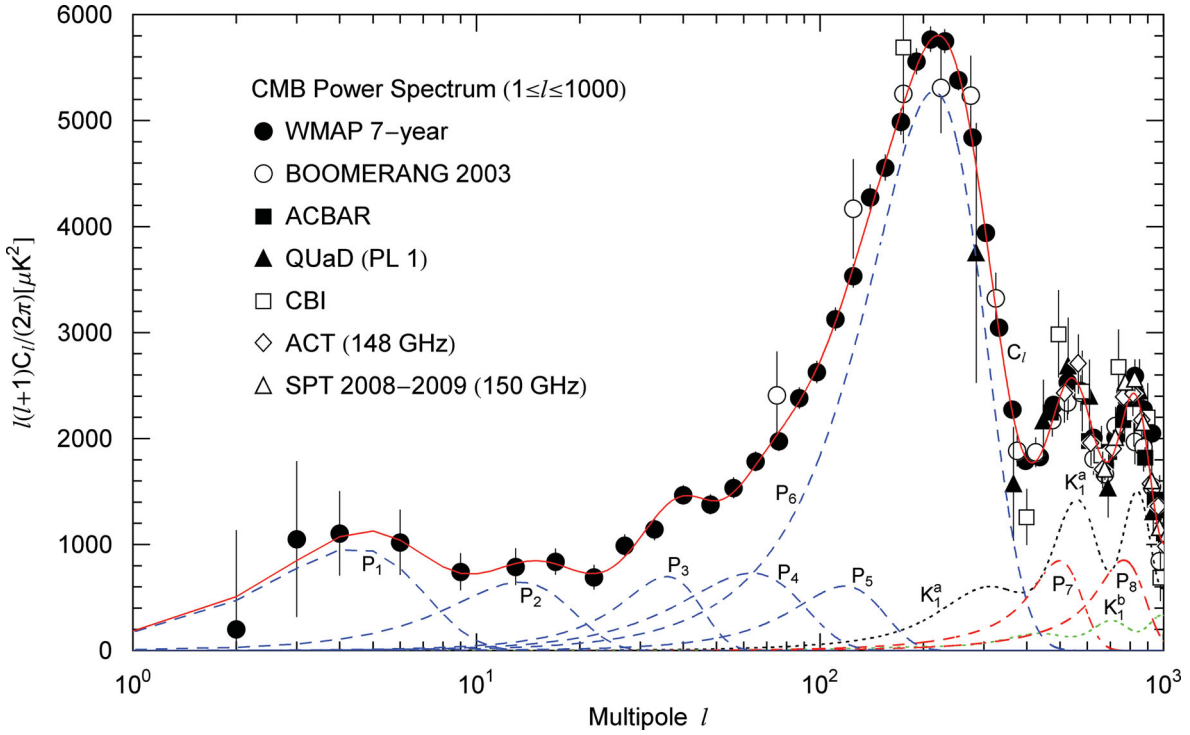

Figure 2. Figs 2–5 are a series of close-ups covering the multipole range depicted in Fig. 1. Data points and notation are the same as given in Fig. 1. The low-l spectrum is composed of five Gaussian peaks $P_{i=1,\dots,5}$ (dashed curves), which additively generate the total moments C_l (solid curve). These peaks have nearly equal height, but do not quite produce a plateau. The main peak of C_l is essentially generated by a single Gaussian component P_6, with small admixtures of the Gaussian peaks P_4, P_5 and P_7, as well as of the oscillatory multipole components K_1^a and K_1^b (dotted curves). The fitting parameters defining the Gaussian peaks $P_{i=1,\dots,8}$ are listed in Table 1.

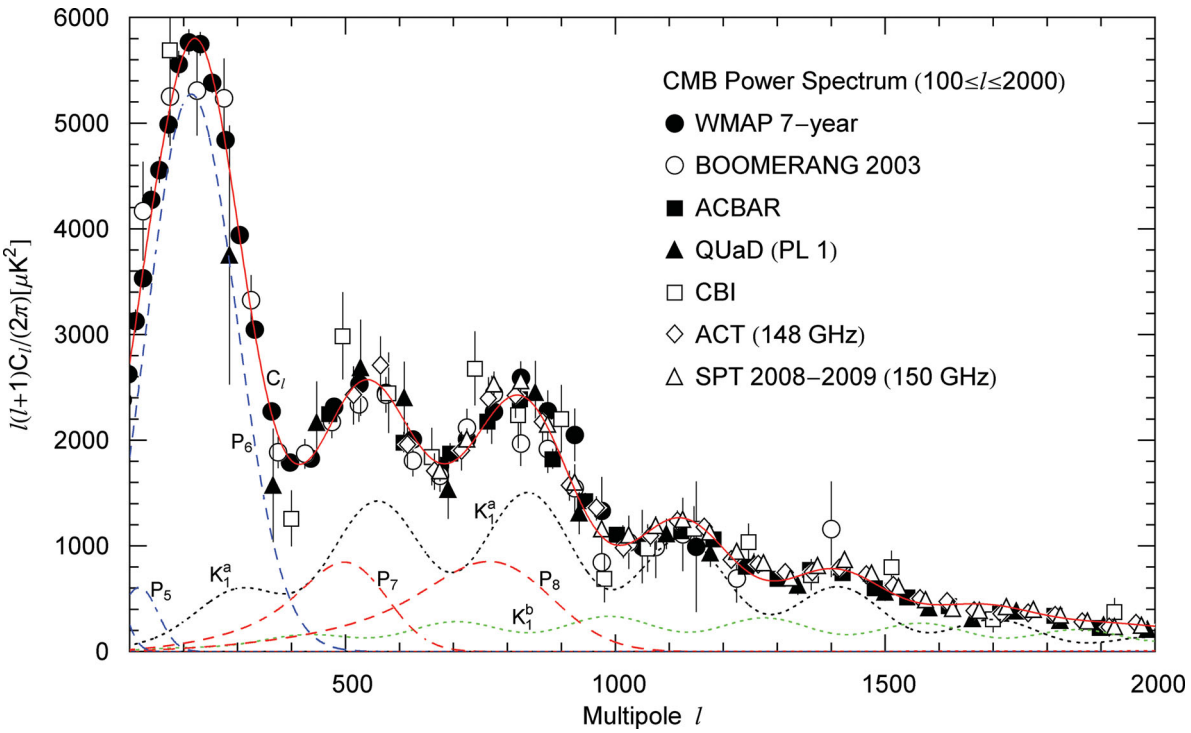

Figure 3. Linear plot of the intermediate multipole regime, depicting the crossover from the Gaussian regime $l \leq 400$ into the oscillatory region $l \geq 1000$. Data points and notation are the same as given in Figs 1 and 2. The fit C_l in the crossover interval $400 \leq l \leq 1000$ consists of two peaks generated by four multipole components, the Gaussian peaks P_7 and P_8 and the oscillatory Kummer distributions K_1^a and K_1^b. The latter are power laws with modulated exponential cut-off, cf. Table 2. The multipole fit in the interval $1000 \leq l \leq 2000$ is essentially produced by the Kummer distributions, $C_l \approx K_1^a + K_1^b$, which admit the same modulation frequency and are shifted in phase, so that their local minima and maxima coincide.

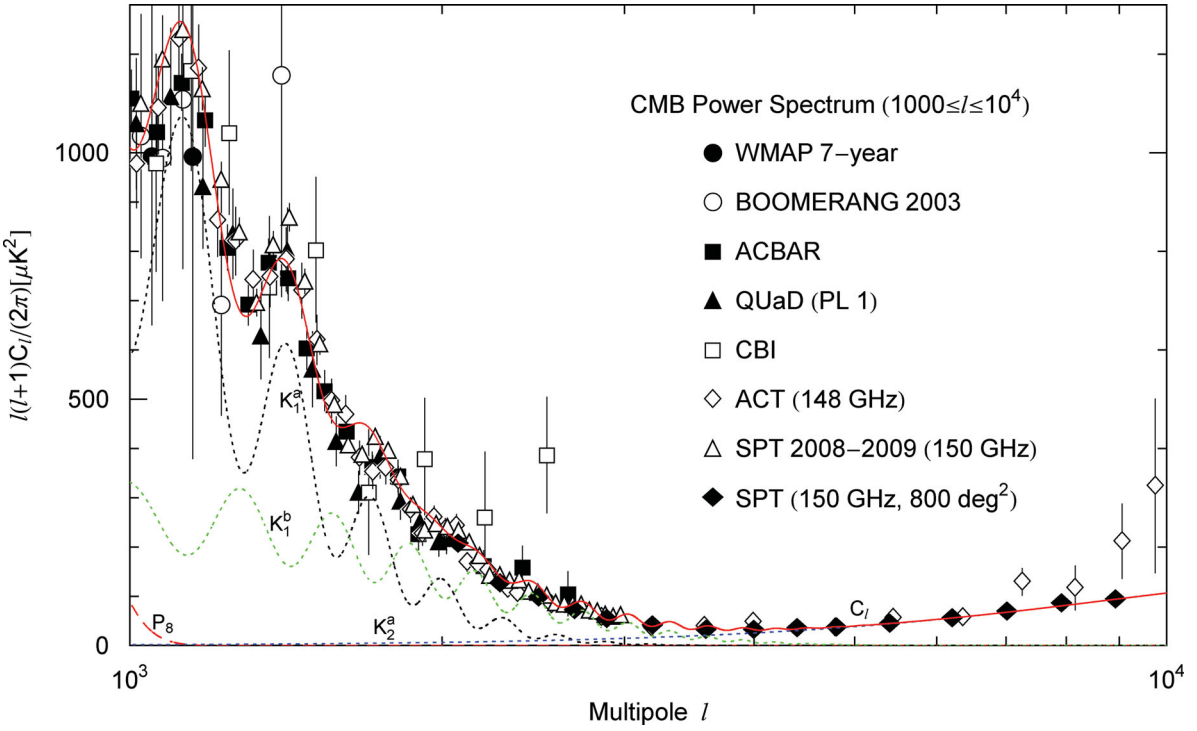

Figure 4. Logarithmic plot of the intermediate and high-l regimes, extending the linear l range of Fig. 2. The C_l moments above $l \sim 10^3$ are generated by the integral kernels listed in Table 2, $C_l \sim K_1^a + K_1^b + K_2^a$. The exponentially decaying distributions K_1^a and K_1^b effectively vanish above $l \sim 4000$. At higher multipoles, the moments C_l increase again, due to a power-law component K_2^a, which emerges at about $l \sim 2000$ and dominates the fit above $l \sim 4000$, $C_l \sim K_2^a$.

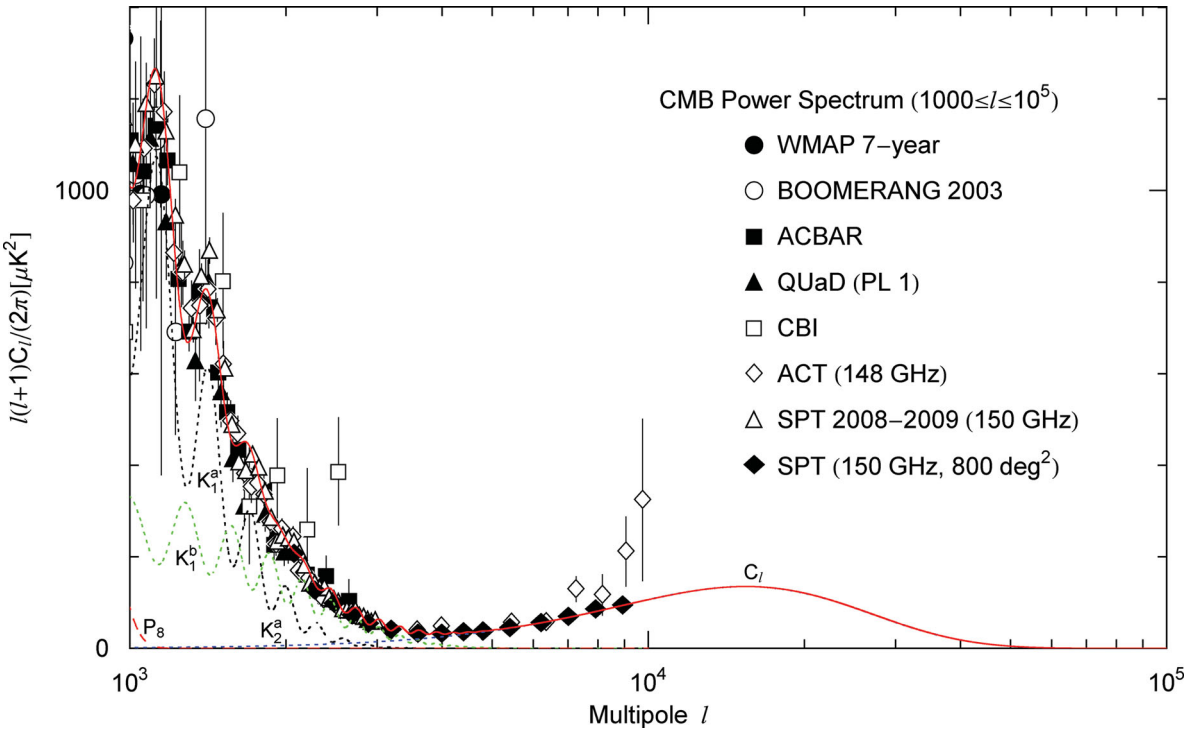

Figure 5. Tail end of the multipole spectrum, extending Fig. 4 by one decade in l. The spectrum above $l \sim 10^4$ is an extrapolation based on SPT data points at 150 GHz. In the range $1000 \leq l \leq 2000$, the multipole moments C_l are produced by Kummer distributions K_1^a and K_1^b, whereas the high-l spectrum above $l \sim 4000$ is dominated by an exponentially decaying power-law component $C_l \sim K_2^a$, which is peaked at $l \approx 15\,400$, with parameters listed in Table 2. A linear close-up of the crossover is shown in Fig. 12, and of the nearly linear power-law slope below $l \sim 10^4$ in Fig. 13.

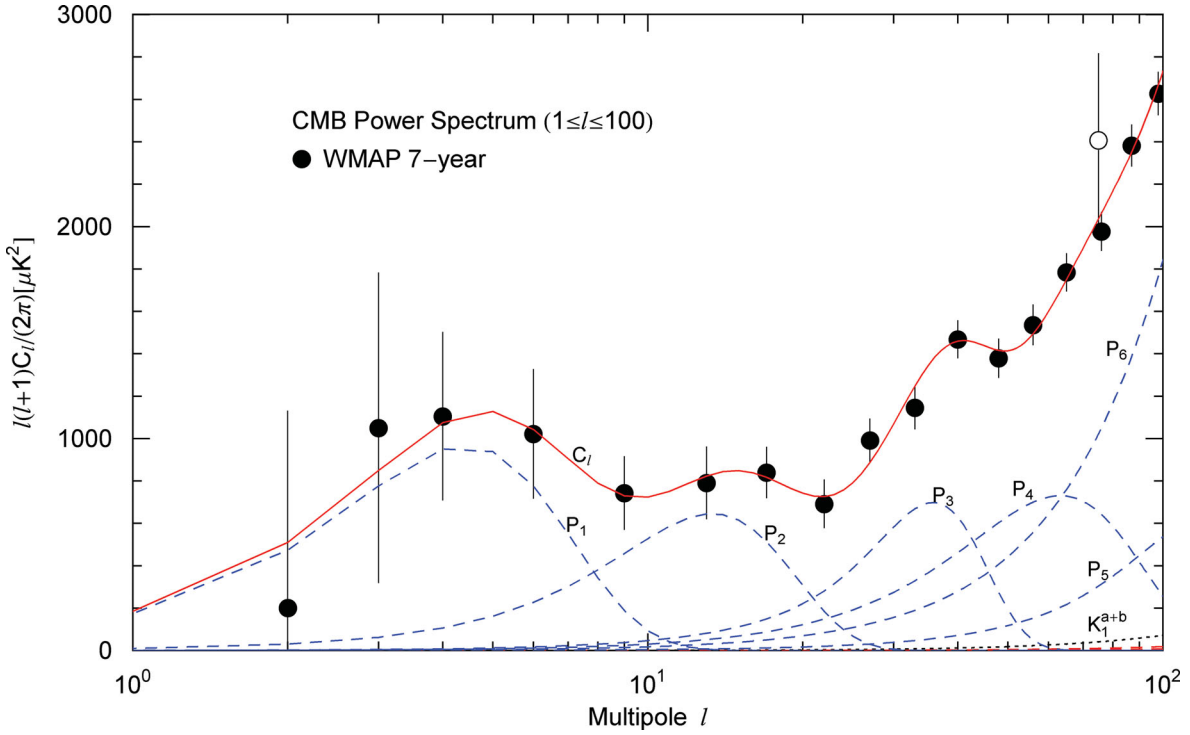

Figure 6. Figs 6 and 7 show logarithmic and linear close-ups of the low-l power spectrum in Fig. 2. The multipole moments C_l located in the l range of this figure are mainly due to Gaussian multipole components P_i. The C_l are additively generated by the Gaussian peaks and the ascending slope of the oscillatory Kummer distribution K_1^{a+b} emerging at the high end of the depicted l range, otherwise the caption of Fig. 2 applies.

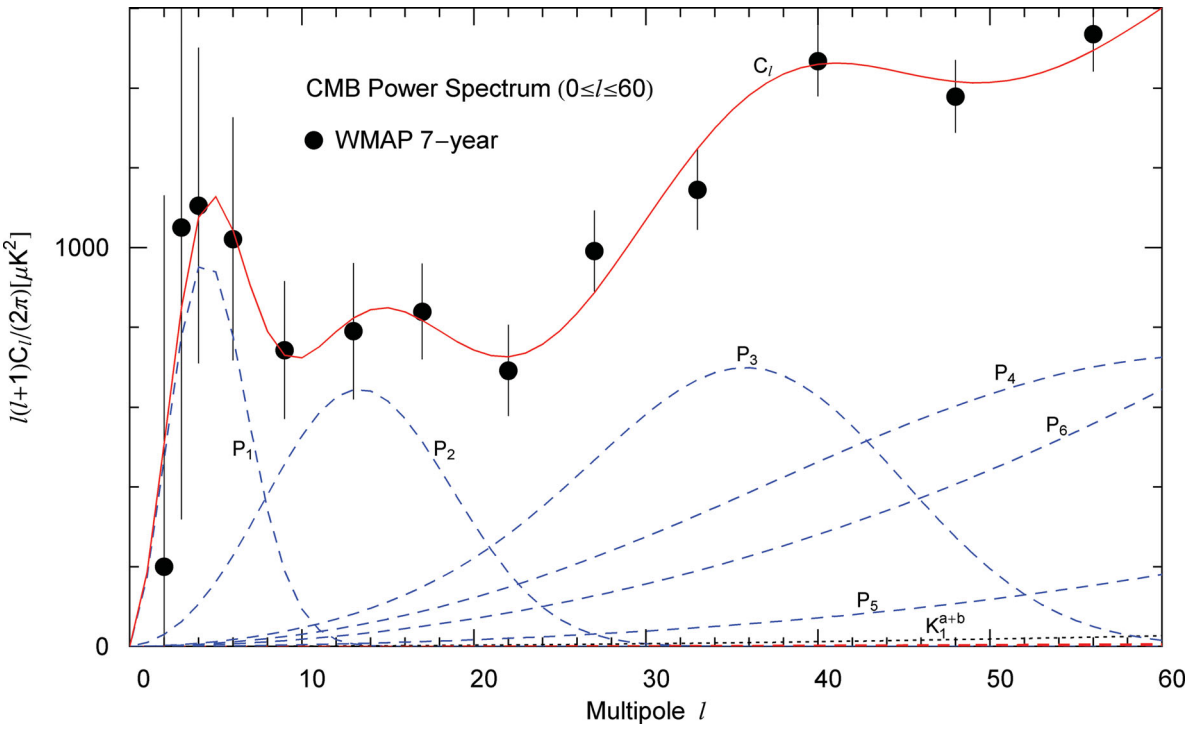

Figure 7. Low-l multipole moments on a linear scale. The C_l moments in this regime are generated by a series of merged Gaussian peaks precursory to the main peak P_6, cf. Fig. 2. The low-l data points have large error bars due to the $1/l$ scaling of the covariance matrix (6.11) (Jarosik et al. 2011; Larson et al. 2011). The total multipole fit C_l and the additive Gaussian components P_i are depicted as polygons (which appear as smooth curves above $l \sim 10$, cf. Fig. 6), only the vertices at integer l are significant. The zeroth coefficient $C_{l=0}$ of the multipole expansion is finite, cf. the integral representation (4.1) and the power-law indices listed in Tables 1 and 2, but does not show in this plot due to the adopted customary $l(l+1)$ normalization, in which the initial slope is ascending.

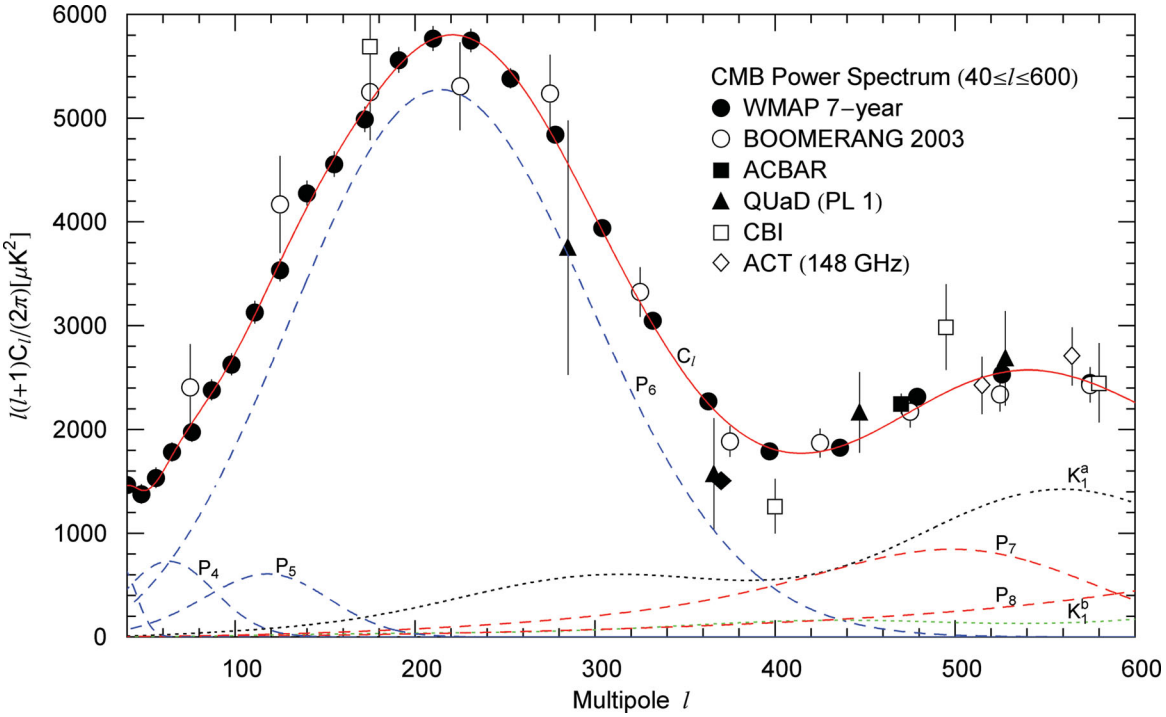

Figure 8. Main peak and onset of the crossover to the oscillatory high-l regime in linear representation. The main peak is essentially Gaussian, composed of the peak P_6 with admixtures of secondary Gaussian components (dashed) and oscillatory Kummer distributions (K_1^a and K_1^b, dotted), cf. Fig. 9. The oscillatory components generate, together with the Gaussian peaks P_7 and P_8 and the decaying fringe of the Gaussian main peak P_6, the multipole moments C_l in the first transitional regime $400 \leq l \leq 1000$, cf. Figs 9 and 10. The fit C_l is obtained by adding the depicted Gaussian and Kummer components, whose integral kernels are specified in Tables 1 and 2.

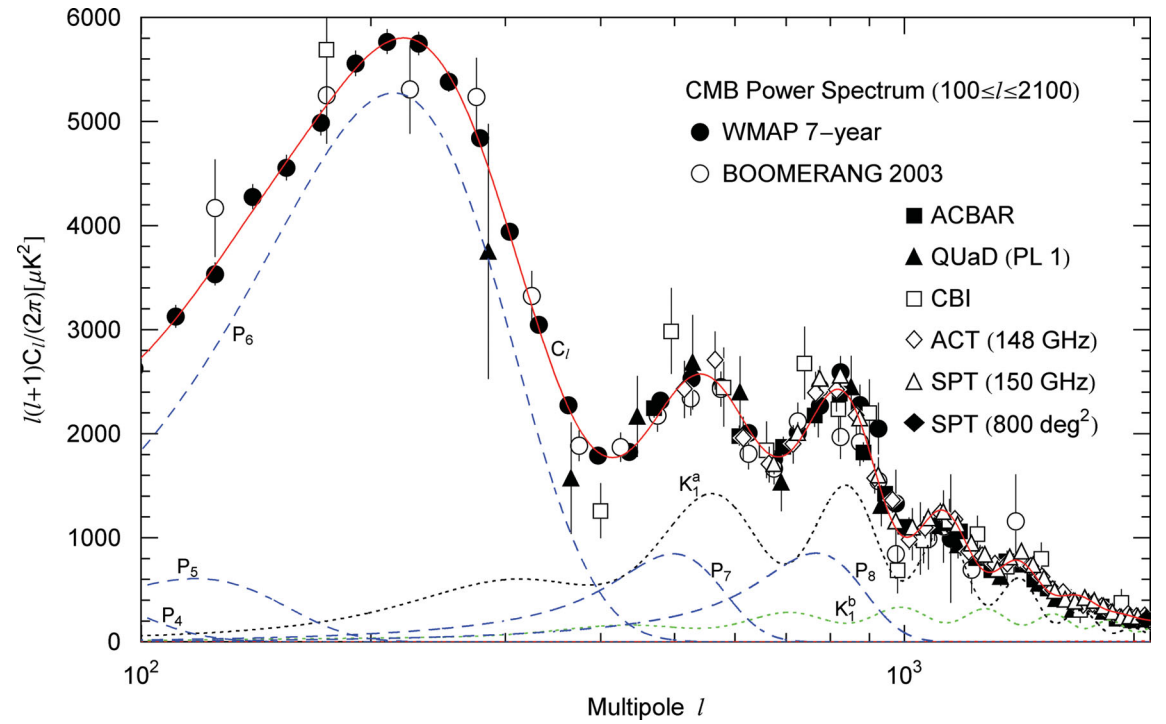

Figure 9. Logarithmic plot of the main peak and the crossover from the Gaussian multipole regime $0 \leq l \leq 400$ to the oscillatory regime $l \geq 10^3$. The peaks above $l \sim 10^3$ are generated by periodic modulations of exponentially cut power-law densities (Kummer distributions). The oscillatory multipole components $K_1^a(l)$ and $K_1^b(l)$ are averages of squared spherical Bessel functions with Kummer distributions, whereas the peaks $P_{i=1,\ldots,8}(l)$ are Gaussian averages. The spectral averaging is explained in Sections 4 and 5.

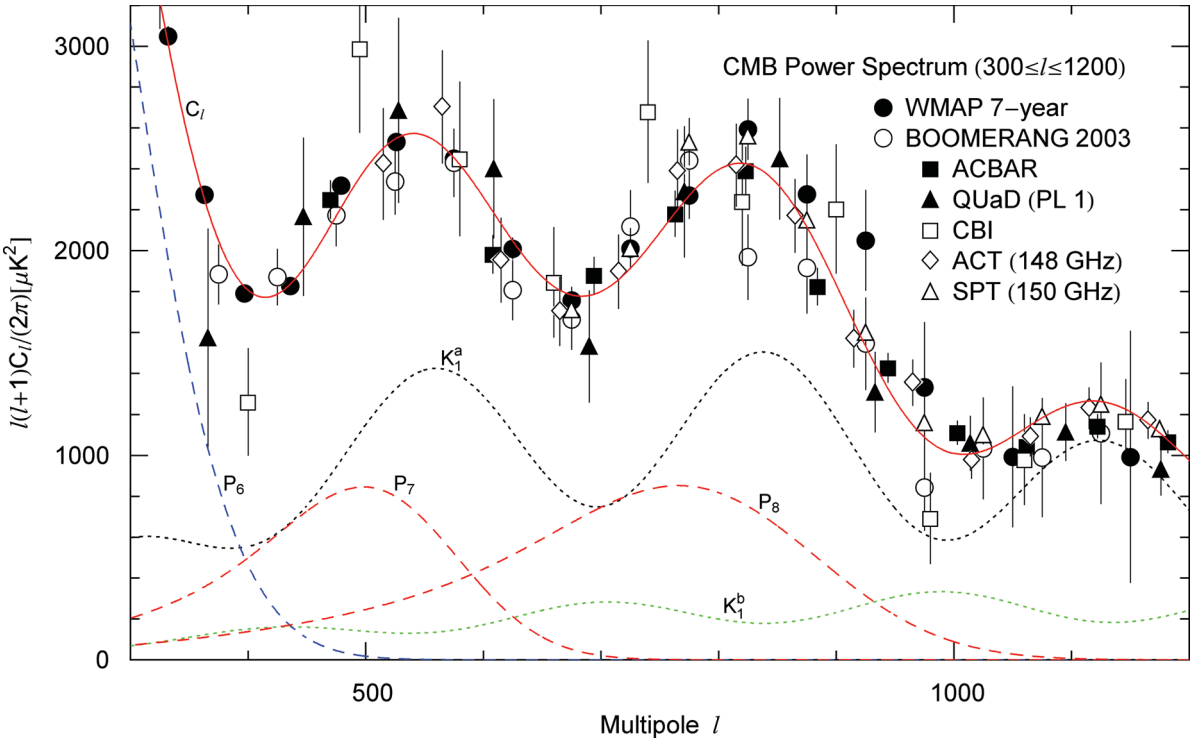

Figure 10. Crossover region $400 \leq l \leq 1000$ between the main peak and the oscillatory multipole regime. The crossover consists of two peaks of nearly equal height and width, generated by the Gaussian peaks P_7 and P_8 and by pronounced modulations in the Kummer distributions K_1^a and K_1^b. The fit of the total moments C_l is obtained by adding the Gaussian (P_i, dashed) and oscillatory ($K_1^{a,b}$, dotted) multipole components.

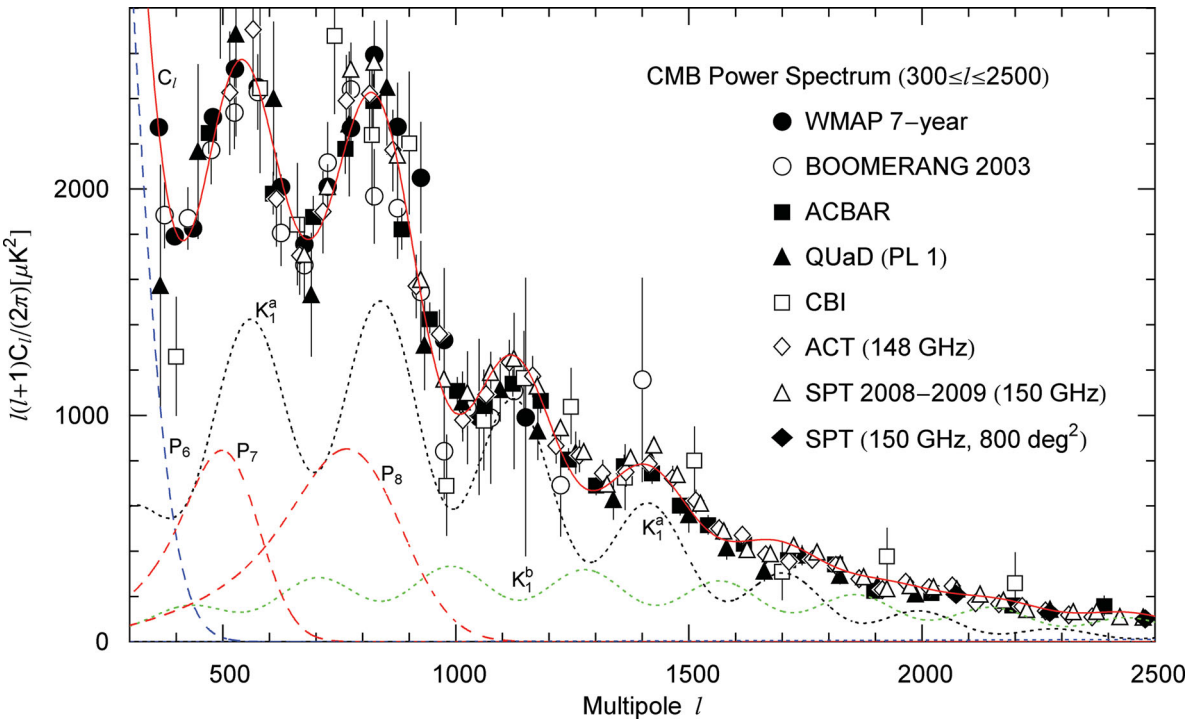

Figure 11. Decaying oscillatory high-l slope. The two transitional peaks in the interval $400 \leq l \leq 1000$ are separated from the oscillatory regime $l \geq 1000$ by a steep descent. In the interval $1000 \leq l \leq 2500$, the multipole moments are determined by two Kummer distributions (dotted curves) additively generating the modulated slope $C_l \approx K_1^a + K_1^b$.

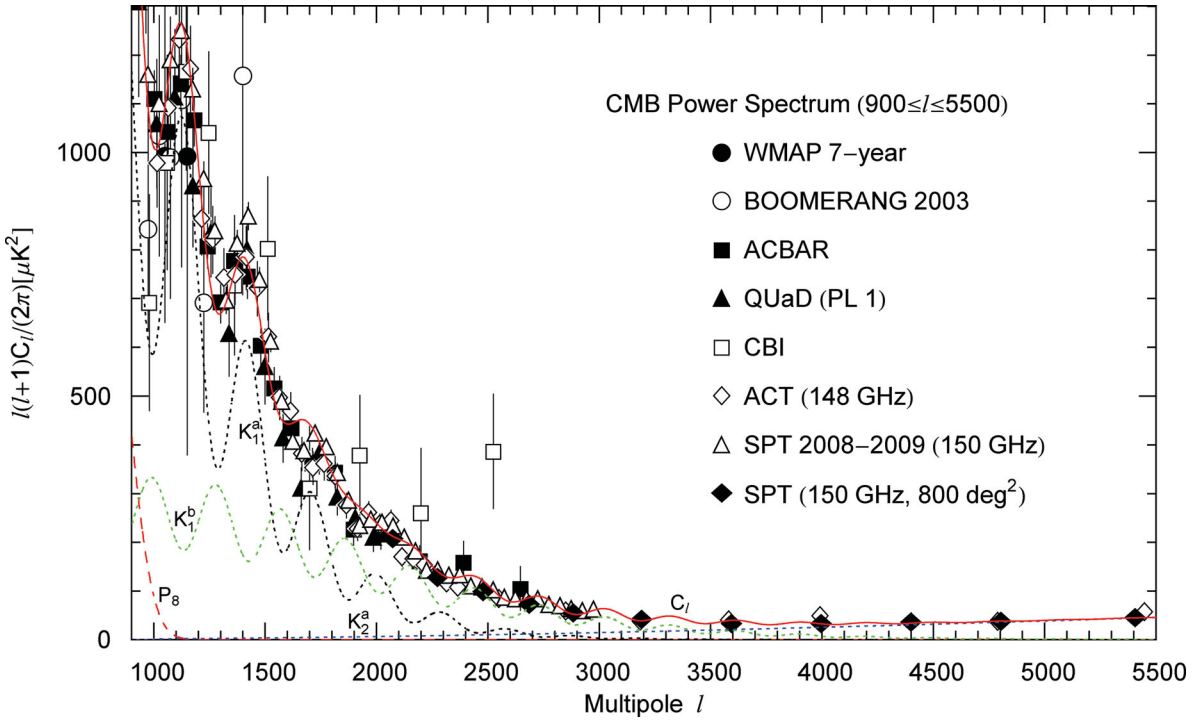

Figure 12. Linear plot of the intermediate and high-l regimes. The decaying oscillatory Kummer distributions K_1^a and K_1^b, which constitute the main contribution to the multipole coefficients C_l in the range $1000 \le l \le 2500$, cf. Fig. 11, become negligible above $l \sim 4000$. A nearly linear multipole component K_2^a (dotted line along the lower edge of this figure) starts to emerge at about $l \sim 2000$. The three Kummer distributions generating the multipole moments $C_l = K_1^a + K_1^b + K_2^a$ in the second crossover regime $2500 \le l \le 4000$ are listed in Table 2. The decaying oscillating tail $K_1^a + K_1^b$ of C_l is gradually replaced by the slowly ascending slope K_2^a of the C_l moments at 150 GHz, which terminates in an extended peak at $l \sim 15\,400$ depicted in Fig. 5.

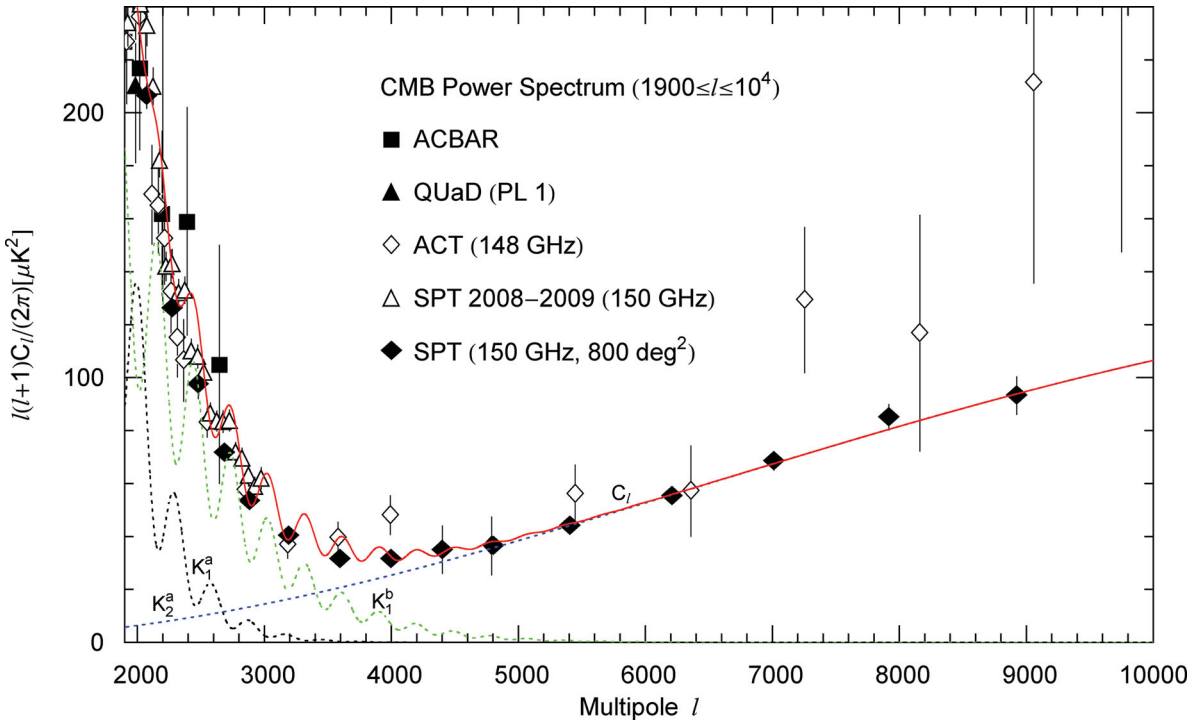

Figure 13. Multipole moments in the high-l regime. The descending modulated slope of C_l is mainly produced by the exponentially damped oscillating components K_1^a and K_1^b, cf. the captions to Figs 4 and 12. The modulation frequency is listed in Table 2. The ascending, nearly linear slope of the C_l moments is generated by the Kummer distribution K_2^a, a power law with exponential cut-off. The four ACT data points above $l = 7000$ have not been included in the spectral fit because of their large error bars and deviation from the SPT points (Das et al. 2011; Reichardt et al. 2012). The logarithmic extrapolation of the fit into the next decade is shown in Fig. 5.

T_b with the cosmic expansion factor, $T_\mathrm{b}(\boldsymbol{p}_0) = T_0[1 + T(\boldsymbol{p}_0)]/a(\tau)$, where $T(\boldsymbol{p}_0)$ stands for the angular fluctuations $\delta T_\mathrm{b}/T_0$. This determines the cosmic time dependence of the distribution function $f(\boldsymbol{p})$; at the present epoch τ_0, the expansion factor can be chosen as $a(\tau_0) = 1$. To preserve the conformal time scaling, we do not assume a time dependence of the fluctuating temperature variable $T(\boldsymbol{p}_0) = \delta T_\mathrm{b}/T_0$, which will be treated as Gaussian random field (scalar and isotropic) on the unit sphere $\boldsymbol{p}_0^2 = 1$.

The following reconstruction of the Green function of the CMB temperature fluctuations does not require any specific cosmological model; it applies irrespectively of the expansion factor, curvature sign and topology of the cosmic 3-space. In this section, we give a self-contained derivation of the two-point autocorrelation function $\langle TT\rangle$ of the spherical random field employed in the multipole fit of the temperature power spectrum in Section 5.

2.1 Legendre expansion of delta distributions on the unit sphere

We start with a Gaussian random field $T(\boldsymbol{p})$ in Euclidean space, and then restrict to the unit sphere $|\boldsymbol{p}| = 1$. The conventions for three-dimensional Fourier transforms are

$$T(\boldsymbol{p}) = \frac{1}{(2\pi)^3}\int \hat{T}(\boldsymbol{k})\mathrm{e}^{\mathrm{i}\boldsymbol{k}\boldsymbol{p}}\mathrm{d}^3k, \quad \hat{T}(\boldsymbol{k}) = \int T(\boldsymbol{p})\mathrm{e}^{-\mathrm{i}\boldsymbol{k}\boldsymbol{p}}\mathrm{d}^3p. \tag{2.1}$$

Reality of $T(\boldsymbol{p})$ requires $\hat{T}(-\boldsymbol{k}) = \hat{T}^*(\boldsymbol{k})$. Fourier transforms are denoted by a hat. The exponential admits a standard expansion in Legendre polynomials (Newton 1982):

$$\mathrm{e}^{\mathrm{i}\boldsymbol{k}\boldsymbol{p}} = \sum_{l=0}^{\infty}\mathrm{i}^l(2l+1)j_l(kp)P_l(\boldsymbol{k}_0\boldsymbol{p}_0). \tag{2.2}$$

Unit vectors are denoted by a subscript zero, $\boldsymbol{k} = k\boldsymbol{k}_0$ and $\boldsymbol{p} = p\boldsymbol{p}_0$. The $j_l(x)$ are spherical Bessel functions, $j_l(x) = \sqrt{\pi/(2x)}J_{1/2+l}(x)$, where $l = 0, 1, 2, \ldots$, and the $P_l(x)$ are Legendre polynomials. We introduce polar coordinates with $\boldsymbol{k}$ or $\boldsymbol{p}$ as polar axis and $0 \le \theta \le \pi$ as polar angle, substitute $\boldsymbol{k}\boldsymbol{p} = kp\cos\theta$ into equation (2.2), and differentiate n times with respect to kp to find

$$(\mathrm{i}\cos\theta)^n\mathrm{e}^{\mathrm{i}kp\cos\theta} = \sum_{l=0}^{\infty}\mathrm{i}^l(2l+1)j_l^{(n)}(kp)P_l(\boldsymbol{k}_0\boldsymbol{p}_0), \tag{2.3}$$

where $\boldsymbol{k}_0\boldsymbol{p}_0 = \cos\theta$. The superscript (n) denotes the nth derivative and $j_l^{(0)} = j_l$. The Poisson integral representation of the spherical Bessel functions in equations (2.2) and (2.3) reads (Magnus, Oberhettinger & Soni 1966)

$$\begin{aligned} j_l(kp) &= \frac{1}{2\mathrm{i}^l}\int_{-1}^{1}\mathrm{e}^{\mathrm{i}kpx}P_l(x)\mathrm{d}x = \frac{1}{2\mathrm{i}^l}\int_0^{\pi}\mathrm{e}^{\mathrm{i}kp\cos\theta}P_l(\cos\theta)\sin\theta\mathrm{d}\theta,\\ j_l^{(n)}(kp) &= \frac{1}{2\mathrm{i}^{l-n}}\int_{-1}^{1}\mathrm{e}^{\mathrm{i}kpx}P_l(x)x^n\mathrm{d}x. \end{aligned} \tag{2.4}$$

The expansion (2.3) thus follows from equation (A5).

We consider the distributions

$$D_{m,n}(\boldsymbol{p}_0,\boldsymbol{q}_0;p,q,k,k') = \int(\mathrm{i}\boldsymbol{k}_0\boldsymbol{p}_0)^m(-\mathrm{i}\boldsymbol{k}_0\boldsymbol{q}_0)^n\mathrm{e}^{\mathrm{i}\boldsymbol{k}_0(kp\boldsymbol{p}_0-k'q\boldsymbol{q}_0)}\mathrm{d}\Omega_{\boldsymbol{k}_0}, \tag{2.5}$$

where $\boldsymbol{k}' = k'\boldsymbol{k}_0$ and $\boldsymbol{q} = q\boldsymbol{q}_0$. The parameters p, q, k and k' are non-negative real numbers. The solid-angle increment indicates integration over the unit sphere; $\mathrm{d}\Omega_{\boldsymbol{k}_0} = \sin\theta\mathrm{d}\theta\mathrm{d}\varphi$, in polar coordinates with polar axis $\boldsymbol{k}_0$, so that $\mathrm{d}^3k = k^2\mathrm{d}k\mathrm{d}\Omega_{\boldsymbol{k}_0}$ in equation (2.1). In equation (2.5), we substitute series (2.3) for $(\mathrm{i}\boldsymbol{k}_0\boldsymbol{p}_0)^m\mathrm{e}^{\mathrm{i}kp\boldsymbol{k}_0\boldsymbol{p}_0}$ and $(-\mathrm{i}\boldsymbol{k}_0\boldsymbol{q}_0)^n\mathrm{e}^{-\mathrm{i}k'q\boldsymbol{k}_0\boldsymbol{q}_0}$. The angular integration can readily be carried out by using the orthogonality relation of Legendre polynomials on the unit sphere, cf. (A3) and (Landau & Lifshitz 1991)

$$\int P_n(\boldsymbol{k}_0\boldsymbol{q}_0)P_l(\boldsymbol{k}_0\boldsymbol{p}_0)\mathrm{d}\Omega_{\boldsymbol{k}_0} = \delta_{nl}\frac{4\pi}{2l+1}P_l(\boldsymbol{p}_0\boldsymbol{q}_0). \tag{2.6}$$

In this way, we obtain the expansion of $D_{m,n}$ in Legendre polynomials,

$$D_{m,n}(\boldsymbol{p}_0,\boldsymbol{q}_0;p,q,k,k') = 4\pi\sum_{l=0}^{\infty}(2l+1)j_l^{(m)}(kp)j_l^{(n)}(k'q)P_l(\boldsymbol{p}_0\boldsymbol{q}_0). \tag{2.7}$$

These distributions are real, and their symmetry properties with regard to a simultaneous interchange of indices and arguments are evident from this expansion. $D_{m,n}$ can be obtained from $D_{0,0}(\boldsymbol{p}_0,\boldsymbol{q}_0;p,q,k,k')$ by multiple differentiation,

$$D_{m,n} = \frac{1}{k^mk'^n}\frac{\mathrm{d}^{m+n}}{\mathrm{d}p^m\mathrm{d}q^n}D_{0,0} = \frac{1}{p^mq^n}\frac{\mathrm{d}^{m+n}}{\mathrm{d}k^m\mathrm{d}k'^n}D_{0,0}. \tag{2.8}$$

We perform a radial integration of $D_{m,n}$, which defines the kernel

$$\Delta_{m,n}(\boldsymbol{p}_0,\boldsymbol{q}_0;p,q) = \frac{1}{(2\pi)^3}\int_0^{\infty}D_{m,n}(\boldsymbol{p}_0,\boldsymbol{q}_0;p,q,k,k)k^{m+n+2}\mathrm{d}k. \tag{2.9}$$

This can also be written as, cf. (2.8),

$$\Delta_{m,n} = \frac{1}{(2\pi)^3}\frac{\mathrm{d}^{m+n}}{\mathrm{d}p^m\mathrm{d}q^n}\int_0^{\infty}D_{0,0}(\boldsymbol{p}_0,\boldsymbol{q}_0;p,q,k,k)k^2\mathrm{d}k. \tag{2.10}$$

Employing the series expansion in equation (2.7), we obtain

$$\Delta_{m,n} = \frac{4\pi}{(2\pi)^3}\sum_{l=0}^{\infty}(-1)^l(2l+1)P_l(\boldsymbol{p}_0\boldsymbol{q}_0)\frac{\mathrm{d}^{m+n}}{\mathrm{d}p^m\mathrm{d}q^n}\int_0^\infty j_l(kp)j_l(kq)k^2\mathrm{d}k. \tag{2.11}$$

Here, the Bessel integral is a representation of the Dirac function (Jackson 1999)

$$\int_0^\infty j_l(kp)j_l(kq)k^2\mathrm{d}k = \frac{\pi}{2q^2}\delta(p-q), \tag{2.12}$$

valid for integer $l \geq 0$ and positive p and q. We use the Legendre representation of the delta function on the unit sphere, cf. (A2) and (A7),

$$\delta_\Omega(\boldsymbol{p}_0, \boldsymbol{q}_0) = \frac{1}{4\pi}\sum_{l=0}^{\infty}(2l+1)P_l(\boldsymbol{p}_0\boldsymbol{q}_0), \tag{2.13}$$

to factorize kernel (2.9),

$$\Delta_{m,n}(\boldsymbol{p}_0, \boldsymbol{q}_0; p, q) = \delta_\Omega(\boldsymbol{p}_0, \boldsymbol{q}_0)\frac{\mathrm{d}^{m+n}}{\mathrm{d}p^m\mathrm{d}q^n}\frac{\delta(p-q)}{q^2}. \tag{2.14}$$

The delta function in Euclidean 3-space can be split as, cf. Appendix A,

$$\delta(p\boldsymbol{p}_0 - q\boldsymbol{q}_0) = \delta_\Omega(\boldsymbol{p}_0, \boldsymbol{q}_0)\frac{\delta(p-q)}{q^2}, \tag{2.15}$$

so that

$$\Delta_{m,n} = \frac{1}{(2\pi)^3}\frac{\mathrm{d}^{m+n}}{\mathrm{d}p^m\mathrm{d}q^n}\int \mathrm{e}^{\mathrm{i}\boldsymbol{k}(p\boldsymbol{p}_0 - q\boldsymbol{q}_0)}\mathrm{d}^3k = \frac{\mathrm{d}^{m+n}}{\mathrm{d}p^m\mathrm{d}q^n}\delta(p\boldsymbol{p}_0 - q\boldsymbol{q}_0). \tag{2.16}$$

This Cartesian representation of kernel (2.9) can directly be recovered from equations (2.5) and (2.10).

2.2 Temperature autocorrelation function

We define the correlation function of the Fourier components $\hat{T}(\boldsymbol{k})$ in equation (2.1) as

$$\hat{G}(\boldsymbol{k}, \boldsymbol{k}') = \langle\hat{T}(\boldsymbol{k})\hat{T}^*(\boldsymbol{k}')\rangle = (2\pi)^3 g_{00}(k)\delta(\boldsymbol{k}-\boldsymbol{k}'). \tag{2.17}$$

Isotropy requires the power spectrum $g_{00}(k)$ to depend only on $k = |\boldsymbol{k}|$, and the delta function reflects homogeneity in Euclidean 3-space, so that the Fourier transform of $\hat{G}(\boldsymbol{k}, \boldsymbol{k}')$ only depends on the distance $\left|\boldsymbol{p} - \boldsymbol{p}'\right|$, cf. (2.21) and (2.25).

In polar coordinates, the Euclidean delta function factorizes as in equation (2.15), so that

$$\langle\hat{T}(\boldsymbol{k})\hat{T}^*(\boldsymbol{k}')\rangle = (2\pi)^3\delta_\Omega(\boldsymbol{k}_0, \boldsymbol{k}_0')g_{00}(k)\frac{\delta(k-k')}{k^2}, \tag{2.18}$$

where δ_Ω denotes the delta function on the unit sphere, cf. Appendix A and equation (2.13). Isotropy is ensured by $\delta_\Omega(\boldsymbol{k}_0, \boldsymbol{k}_0')$, which is the only angular dependent factor. We abandon homogeneity (since the random field will ultimately be restricted to the unit sphere) by replacing the singular radial factor $g_{00}(k)\delta(k-k')/k^2$ by a more general kernel function,

$$\hat{G}(\boldsymbol{k}_0, \boldsymbol{k}_0'; k, k') := \langle\hat{T}(\boldsymbol{k})\hat{T}^*(\boldsymbol{k}')\rangle = (2\pi)^3\delta_\Omega(\boldsymbol{k}_0, \boldsymbol{k}_0')\frac{\Delta(k, k')}{k^2k'^2}, \tag{2.19}$$

where $\boldsymbol{k} = k\boldsymbol{k}_0$, $\boldsymbol{k}' = k'\boldsymbol{k}_0'$ and

$$\Delta(k, k') = \sum_{m,n=0}^{N-1}(-1)^{m+n}\frac{\mathrm{d}^{m+n}}{\mathrm{d}k^m\mathrm{d}k'^n}\left(g_{mn}(k)k^2\delta(k-k')\right). \tag{2.20}$$

Here, $g_{mn}(k)$ is an N-dimensional matrix, which will be chosen as positive-definite or semidefinite Hermitian. At this stage, we do not impose any symmetry requirements on $g_{mn}(k)$, which is thus an arbitrary complex $N \times N$ matrix. The homogeneous case (2.18) corresponds to $N = 1$.

The Fourier transform of the two-point function (2.19) is defined as

$$G(\boldsymbol{p}_0, \boldsymbol{p}_0'; p, p') := \langle T(\boldsymbol{p})T(\boldsymbol{p}')\rangle = \frac{1}{(2\pi)^6}\iint\langle\hat{T}(\boldsymbol{k})\hat{T}^*(\boldsymbol{k}')\rangle\mathrm{e}^{\mathrm{i}\boldsymbol{k}\boldsymbol{p}}\mathrm{e}^{-\mathrm{i}\boldsymbol{k}'\boldsymbol{p}'}\mathrm{d}^3k\mathrm{d}^3k', \tag{2.21}$$

where $\boldsymbol{p} = p\boldsymbol{p}_0$ and $\boldsymbol{p}' = p'\boldsymbol{p}_0'$. Zero subscripts denote unit vectors. We may write this as

$$\langle T(\boldsymbol{p})T(\boldsymbol{p}')\rangle = \frac{1}{(2\pi)^3}\int_0^\infty\mathrm{d}k\int_0^\infty\mathrm{d}k'\int\mathrm{d}\Omega_{k_0}\int\mathrm{d}\Omega_{k_0'}\delta_\Omega(\boldsymbol{k}_0, \boldsymbol{k}_0')\Delta(k, k')\mathrm{e}^{\mathrm{i}kp\boldsymbol{k}_0\boldsymbol{p}_0 - \mathrm{i}k'p'\boldsymbol{k}_0'\boldsymbol{p}_0'}. \tag{2.22}$$

One of the angular integrations can readily be carried out by virtue of the delta function, cf. (2.5),

$$\langle T(\boldsymbol{p})T(\boldsymbol{p}')\rangle = \frac{1}{(2\pi)^3}\int_0^\infty\mathrm{d}k\int_0^\infty\mathrm{d}k'\Delta(k, k')D_{0,0}(\boldsymbol{p}_0, \boldsymbol{p}_0'; p, p', k, k'). \tag{2.23}$$

We substitute $\Delta(k, k')$ in equation (2.20), perform the partial integrations, use equation (2.8) and perform one integration by means of the delta function, to find the representation

$$\langle T(\boldsymbol{p})T(\boldsymbol{p}')\rangle = \sum_{m,n=0}^{N-1}\frac{p^mp'^n}{(2\pi)^3}\frac{\mathrm{d}^{m+n}}{\mathrm{d}p^m\mathrm{d}p'^n}\int_0^\infty\mathrm{d}k\frac{g_{mn}(k)}{k^{m+n-2}}D_{0,0}(\boldsymbol{p}_0, \boldsymbol{p}_0'; p, p', k, k). \tag{2.24}$$

There are several ways to proceed. First, we may substitute

$$D_{0,0}(\boldsymbol{p}_0, \boldsymbol{p}'_0; p, p', k, k) = \int \mathrm{e}^{\mathrm{i}k\boldsymbol{k}_0(p\boldsymbol{p}_0 - p'\boldsymbol{p}'_0)}\mathrm{d}\Omega_{\boldsymbol{k}_0} = \frac{4\pi}{kr}\sin(kr), \quad r = \sqrt{p^2 + p'^2 - 2pp'\cos\theta}, \quad \boldsymbol{p}_0\boldsymbol{p}'_0 = \cos\theta. \tag{2.25}$$

Alternatively, we may use equation (2.8) to write (2.24) as

$$\langle T(\boldsymbol{p})T(\boldsymbol{p}')\rangle = \sum_{m,n=0}^{N-1}\frac{p^m p'^n}{(2\pi)^3}\int_0^\infty \mathrm{d}k k^2 g_{mn}(k) D_{m,n}(\boldsymbol{p}_0, \boldsymbol{p}'_0; p, p', k, k). \tag{2.26}$$

Finally, we may substitute the Legendre expansion (2.7) of $D_{0,0}$ into equation (2.24) to find

$$G(\boldsymbol{p}_0, \boldsymbol{p}'_0; p, p') = \langle T(\boldsymbol{p})T(\boldsymbol{p}')\rangle = \frac{1}{4\pi}\sum_{l=0}^\infty (2l+1)C_l(p, p')P_l(\boldsymbol{p}_0\boldsymbol{p}'_0), \tag{2.27}$$

where we identified the multipole moments as

$$C_l(p, p') = \frac{2}{\pi}\int_0^\infty \mathrm{d}k \int_0^\infty \mathrm{d}k' \Delta(k, k') j_l(kp) j_l(k'p'). \tag{2.28}$$

One of the radial integrations in equation (2.28) is carried out by means of the delta function in $\Delta(k, k')$, cf. (2.20), and we find, by multiple partial integration,

$$C_l(p, p') = \frac{2}{\pi}\sum_{m,n=0}^{N-1} p^m p'^n \int_0^\infty g_{mn}(k) j_l^{(m)}(kp) j_l^{(n)}(kp') k^2 \mathrm{d}k. \tag{2.29}$$

This representation (equations 2.27–2.29) of the Green function can be recovered by substituting the Legendre expansion (2.7) of $D_{m,n}$ into (2.26).

We denote the two-point function (2.27) by $G(\boldsymbol{p}_0, \boldsymbol{p}'_0; p, p')$, regarding it as an isotropic kernel on the unit sphere depending on the angle $\boldsymbol{p}_0\boldsymbol{p}'_0 = \cos\theta$ and two arbitrary positive scale-parameters p and p', cf. (2.19) and (2.21). The symmetry properties of $G(\boldsymbol{p}_0, \boldsymbol{p}'_0; p, p')$ with respect to p and p' depend on the coefficients $C_l(p, p')$ in equation (2.29). The $C_l(p, p')$ are symmetric in p and p' if the matrix $g_{mn}(k)$ is symmetric, and they are real if $g_{mn}(k)$ is real. If the matrix $g_{mn}(k)$ is Hermitian, we find $C_l(p, p') = C_l^*(p', p)$. These symmetries of $C_l(p, p')$ are inherited by the Green function $G(\boldsymbol{p}_0, \boldsymbol{p}'_0; p, p')$.

If $p' = p$ (which will be assumed in the sequel), we write $C_l(p)$ or simply C_l for $C_l(p, p)$ in equation (2.29) and $G(\boldsymbol{p}_0, \boldsymbol{p}'_0; p)$ or $G(\boldsymbol{p}_0, \boldsymbol{p}'_0)$ for the correlation function $G(\boldsymbol{p}_0, \boldsymbol{p}'_0; p, p)$ in equation (2.27). The coefficients $C_l(p)$ are real if $g_{mn}(k)$ is Hermitian or an arbitrary real matrix. Positivity of $C_l(p)$ is ensured if $g_{mn}(k)$ is a positive-definite Hermitian (or real symmetric) matrix. The condition $C_l(p) \geq 0$ is satisfied if $g_{mn}(k)$ is semidefinite. Thus, $G(\boldsymbol{p}_0, \boldsymbol{p}'_0; p)$ is a positive (semi)definite kernel on the unit sphere if $g_{mn}(k)$ is a positive (semi)definite Hermitian matrix. Reality, symmetry and positive definiteness are the requirements for $G(\boldsymbol{p}_0, \boldsymbol{p}'_0; p)$ to be a Gaussian correlation function, cf. Section 6.

3 MULTIPOLE MOMENTS OF ISOTROPIC GAUSSIAN RANDOM FIELDS ON THE UNIT SPHERE

3.1 Hermitian spectral matrices defining angular power spectra

The Green function (2.27) is defined by multipole moments depending on a positive-definite or semidefinite Hermitian $N \times N$ matrix $g_{mn}(k)$, $m, n = 0, \ldots, N-1$, and a scale parameter p,

$$G(\boldsymbol{p}_0, \boldsymbol{p}'_0; p, g_{mn}) = \frac{1}{4\pi}\sum_{l=0}^\infty (2l+1)C_l^{(N)}(p)P_l(\boldsymbol{p}_0\boldsymbol{p}'_0),$$
$$C_l^{(N)}(p) = \frac{2}{\pi}\sum_{m,n=0}^{N-1} p^{m+n}\int_0^\infty g_{mn}(k) j_l^{(m)}(kp) j_l^{(n)}(kp) k^2 \mathrm{d}k. \tag{3.1}$$

Multiple derivatives of the spherical Bessel functions $j_l(x)$ are indicated by superscripts (m) and (n). We will also occasionally use a superscript (N) for the matrix dimension, mainly $N = 1$ and 2 in this paper. The case $N = 1$ can readily be settled; we write $P(k)$ for density $g_{00}^{(N=1)}(k) \geq 0$ to obtain the moments (3.1) as

$$C_l^{(N=1)}(p) = \frac{2}{\pi}\int_0^\infty P(k) j_l^2(kp) k^2 \mathrm{d}k. \tag{3.2}$$

As for $N = 2$, we factorize the 2×2 matrix $g_{mn}(k)$ as

$$g_{mn}^{(N=2)}(k) = \mathbf{U}^{-1}\mathrm{diag}(A, B)\mathbf{U}, \tag{3.3}$$

where the diagonal matrix is defined by real constants $A \geq 0$, $B \geq 0$, and $\mathbf{U}$ is a unitary matrix of determinant 1, parametrized as

$$\mathbf{U}(\theta, \psi, \chi) = \begin{pmatrix} \mathrm{e}^{\mathrm{i}\psi}\cos\theta & \mathrm{e}^{\mathrm{i}\chi}\sin\theta \\ -\mathrm{e}^{-\mathrm{i}\chi}\sin\theta & \mathrm{e}^{-\mathrm{i}\psi}\cos\theta \end{pmatrix}, \quad \mathbf{U}^{-1} = \begin{pmatrix} \mathrm{e}^{-\mathrm{i}\psi}\cos\theta & -\mathrm{e}^{\mathrm{i}\chi}\sin\theta \\ \mathrm{e}^{-\mathrm{i}\chi}\sin\theta & \mathrm{e}^{\mathrm{i}\psi}\cos\theta \end{pmatrix}, \tag{3.4}$$

so that $\mathbf{U}^{-1}(\theta,\psi,\chi)=\mathbf{U}(-\theta,-\psi,\chi)$. The Hermitian $g_{mn}(k)$ thus reads

$$g_{mn}(k)=\begin{pmatrix} A\cos^2\theta+B\sin^2\theta & (A-B)\mathrm{e}^{\mathrm{i}(\chi-\psi)}\sin\theta\cos\theta \\ (A-B)\mathrm{e}^{-\mathrm{i}(\chi-\psi)}\sin\theta\cos\theta & A\sin^2\theta+B\cos^2\theta \end{pmatrix}, \tag{3.5}$$

with $m,n=0,1$ and $\det g_{mn}=AB$. This parametrization covers all two-dimensional positive semidefinite Hermitian matrices. $g_{mn}(k)$ depends on four independent real parameters (A,B,θ,φ), where $\varphi=(\chi-\psi)/2$. These four parameters can be arbitrary real functions of the spectral variable k. The case $\varphi=0$ is just a rotation in the Euclidean plane, resulting in a real symmetric matrix. In higher dimensions, $N\geq 3$, we use subgroups $U_i(\theta_i,\psi_i,\chi_i)$ as in equation (3.4) to obtain an Euler-type parametrization of the Hermitian matrix, cf. Appendix B. In the case that $g_{mn}(k)$ factorizes as $h_m(k)h_n^*(k)$, we can substitute in equation (3.1)

$$\sum_{m,n=0}^{N-1} p^{m+n}g_{mn}(k)j_l^{(m)}(kp)j_l^{(n)}(kp)=\left|\sum_{m=0}^{N-1}p^m h_m(k)j_l^{(m)}(kp)\right|^2. \tag{3.6}$$

More generally, we can always split this quadratic form into a sum of N squares by diagonalization as in equation (3.3). In two dimensions, cf. (3.5),

$$\begin{aligned}
&\sum_{m,n=0,1} p^{m+n}g_{mn}(k)j_l^{(m)}(kp)j_l^{(n)}(kp)=g_l^A(k,p)+g_l^B(k,p),\\
&g_l^A(k,p)=A(k)\left|\cos\theta(k)j_l(kp)+\sin\theta(k)\,\mathrm{e}^{2\mathrm{i}\varphi(k)}pj_l'(kp)\right|^2,\\
&g_l^B(k,p)=B(k)\left|\sin\theta(k)j_l(kp)-\cos\theta(k)\,\mathrm{e}^{2\mathrm{i}\varphi(k)}pj_l'(kp)\right|^2,
\end{aligned} \tag{3.7}$$

where we have put $\chi-\psi=2\varphi$. Here, the vectors $h_m(k)$ defining the squares in equation (3.7) are just the rows of matrix $\mathbf{U}$ in equation (3.4), multiplied with a convenient phase factor and the root of the respective coefficient in the diagonal matrix in equation (3.3); the same holds for higher dimensions. A diagonal $g_{mn}^{(N)}(k)$ results in a series of squared derivatives $j_l^{(n)}$. Positive definiteness of $g_{mn}^{(N=2)}(k)$ requires $A>0$ as well as $B>0$.

According to equation (3.7), the multipole coefficients $C_l^{(N=2)}(p)$ in equation (3.1) can be decomposed as

$$C_l^{(N=2)}(p)=C_l^A(p)+C_l^B(p), \tag{3.8}$$

$$C_l^A(p)=\frac{2}{\pi}\int_0^\infty g_l^A(k,p)k^2\mathrm{d}k,\quad C_l^B(p)=\frac{2}{\pi}\int_0^\infty g_l^B(k,p)k^2\mathrm{d}k, \tag{3.9}$$

where

$$\begin{aligned}
g_l^A(k,p)&=A\left(\cos^2\theta\, j_l^2+\sin^2\theta\, p^2 j_l'^2+2\cos 2\varphi\sin\theta\cos\theta\, pj_l j_l'\right),\\
g_l^B(k,p)&=B\left(\sin^2\theta\, j_l^2+\cos^2\theta\, p^2 j_l'^2-2\cos 2\varphi\sin\theta\cos\theta\, pj_l j_l'\right).
\end{aligned} \tag{3.10}$$

The argument of the Bessel functions is kp, and the amplitudes and angles A, B, θ and φ depend on the spectral variable k as indicated in equation (3.7). If we put $\chi-\psi=2\varphi=\pi/2$ in matrix (3.5), the mixed terms $j_l j_l'$ drop out.

When performing the integrations (3.9), it is convenient to write the spectral functions (3.10) linear in the harmonics,

$$\begin{aligned}
g_l^A(k,p)&=\frac{A}{2}\Big[(1+\cos 2\theta)j_l^2(kp)+(1-\cos 2\theta)p^2 j_l'^2(kp)\\
&\quad+(\sin 2(\theta+\varphi)+\sin 2(\theta-\varphi))\,pj_l(kp)j_l'(kp)\Big],\\
g_l^B(k,p)&=\frac{B}{2}\Big[(1-\cos 2\theta)j_l^2(kp)+(1+\cos 2\theta)p^2 j_l'^2(kp)\\
&\quad-(\sin 2(\theta+\varphi)+\sin 2(\theta-\varphi))\,pj_l(kp)j_l'(kp)\Big].
\end{aligned} \tag{3.11}$$

We note that $g_l^A(k,p)$ and $g_l^B(k,p)$ only differ by a change of sign of the harmonics, apart from the amplitudes A and B, and do not depend on the sign of the angle φ. The amplitudes $A(k)$ and $B(k)$ as well as the angles $\theta(k)$ and $\varphi(k)$ will be specified in equations (3.15) and (3.16).

We consider linear combinations of the Green functions $G(\boldsymbol{p}_0,\boldsymbol{p}_0';p,g_{mn})$ in equation (3.1),

$$G(\boldsymbol{p}_0,\boldsymbol{p}_0';p)=\sum_{g_{mn}}G(\boldsymbol{p}_0,\boldsymbol{p}_0';p,g_{mn})=\frac{1}{4\pi}\sum_{l=0}^\infty(2l+1)C_l(p)P_l(\boldsymbol{p}_0\boldsymbol{p}_0'), \tag{3.12}$$

where the summation is taken over a set of one- and two-dimensional matrices $g_{mn}(k)$. The multipole coefficients $C_l(p)$ in equation (3.12) are obtained by adding the coefficients $C_l^{(N)}(p)$ of the respective components $G(\boldsymbol{p}_0,\boldsymbol{p}_0';p,g_{mn})$, cf. (3.1). For instance, on adding $C_l^{(N=1)}$ in equation (3.2) and $C_l^{(N=2)}$ in equations (3.8) and (3.9), we find

$$\begin{aligned}
&C_l(p)=C_l^{(N=1)}(p)+C_l^{(N=2)}(p),\quad C_l^{(N=2)}(p)=C_l^A(p)+C_l^B(p),\\
&C_l^{(N=1)}(p)=\frac{2}{\pi}\int_0^\infty P(k)j_l^2(kp)k^2\mathrm{d}k,\quad C_l^{A,B}(p)=\frac{2}{\pi}\int_0^\infty g_l^{A,B}(k,p)k^2\mathrm{d}k.
\end{aligned} \tag{3.13}$$

As for the integral kernels, $P(k)$ is a density specified in equation (3.14), and the spectral functions $g_l^A(k, p)$ and $g_l^B(k, p)$ are stated in equation (3.11), with angular parametrization (3.15) and amplitudes (3.16). More generally, any Green function (3.12) obtained by summation over a finite set of positive (semi)definite Hermitian matrices $g_{mn}^{(N)}(k)$ (of the same or varying dimension N) is a positive-definite or semidefinite Hermitian kernel, and the same holds for linear combinations with positive coefficients. We may also use different scale parameters p in each of the component functions $G(\boldsymbol{p}_0, \boldsymbol{p}'_0; p, g_{mn})$ in equation (3.12). In the following, we will perform a summation over one- and two-dimensional matrices as in equation (3.13), using the same scale parameter p in each component $G(\boldsymbol{p}_0, \boldsymbol{p}'_0; p, g_{mn})$.

3.2 Spectral parametrization of multipole moments: Gaussian power-law densities and Kummer distributions

As for the coefficients $C_l^{(N=1)}(p)$ in equation (3.2), we parametrize the kernel $P(k)$ with a series of Gaussian power-law densities,

$$P(k) = \sum_i P_i(k), \quad P_i(k) = a_{0,i} k^{\mu_{0,i}} \mathrm{e}^{-\alpha_{0,i} k^2 - \beta_{0,i} k}, \tag{3.14}$$

with amplitudes $a_{0,i} > 0$ and real exponents $\mu_{0,i}$, $\beta_{0,i}$, and $\alpha_{0,i} > 0$. This series corresponds to a summation over a set of one-dimensional matrices in equation (3.12).

Regarding the coefficients $C_l^{(N=2)}(p)$ in equation (3.8), we need to specify the k dependence of the angles and amplitudes in the 2×2 matrix (3.5) and the associated spectral functions $g_l^{A,B}(k, p)$ in (3.11). We use a linear k parametrization of the angles,

$$\theta(k) = \frac{1}{2}(\omega k + \theta_0), \quad \varphi(k) = \frac{1}{2}(\chi - \psi) = \frac{1}{2}(\omega_0 k + \varphi_0), \tag{3.15}$$

where ω, θ_0, ω_0 and φ_0 are real constants. When performing the CMB temperature fit, it suffices to put $\theta_0 = 0$ and $\varphi(k) = 0$ from the outset. The amplitudes are Gaussian power laws like in equation (3.14),

$$A(k) = 2ak^{\mu_1} \mathrm{e}^{-\alpha_1 k^2 - \beta_1 k}, \quad B(k) = 2bk^{\mu_2} \mathrm{e}^{-\alpha_2 k^2 - \beta_2 k}, \tag{3.16}$$

with $a \geq 0$, $b \geq 0$ and real exponents $\mu_{1,2}$, $\beta_{1,2}$ and $\alpha_{1,2}$. In the CMB temperature fit, we use $\alpha_{1,2} = 0$ and $\beta_{1,2} > 0$, that is, power-law densities with exponential cut-off. If the amplitudes a and b in equation (3.16) have opposite sign, the Hermitian spectral matrix (3.5) is indefinite, but the multipole coefficients $C_l^{(N=2)}(p)$ in equation (3.13) can still be positive for all l. Similarly, if some of the Gaussian amplitudes $a_{0,i}$ in equation (3.14) are negative, the total moments $C_l(p)$ in equation (3.13) can still be positive. Positivity of the amplitudes is sufficient but not necessary to ensure a positive-definite kernel (3.12).

On substituting the angles (3.15) and amplitudes (3.16) into the spectral functions $g_l^{A,B}(k, p)$ in equation (3.11), we find

$$g_l^A(k, p) = g_l^{A(0,0)} + p g_l^{A(0,1)} + p^2 g_l^{A(1,1)}, \quad g_l^B(k, p) = g_l^{B(0,0)} + p g_l^{B(0,1)} + p^2 g_l^{B(1,1)}, \tag{3.17}$$

where $g_l^{A(0,0)}$ and $g_l^{B(0,0)}$ denote the terms depending on $j_l^2(kp)$ in equation (3.11),

$$\begin{aligned} g_l^{A(0,0)} &= ak^{\mu_1} \mathrm{e}^{-\alpha_1 k^2 - \beta_1 k} j_l^2(kp)[1 + \mathrm{Re}(\mathrm{e}^{-\mathrm{i}\omega k}) \cos\theta_0 + \mathrm{Im}(\mathrm{e}^{-\mathrm{i}\omega k}) \sin\theta_0], \\ g_l^{B(0,0)} &= bk^{\mu_2} \mathrm{e}^{-\alpha_2 k^2 - \beta_2 k} j_l^2(kp)[1 - \mathrm{Re}(\mathrm{e}^{-\mathrm{i}\omega k}) \cos\theta_0 - \mathrm{Im}(\mathrm{e}^{-\mathrm{i}\omega k}) \sin\theta_0]. \end{aligned} \tag{3.18}$$

The terms $g_l^{A(1,1)}$ and $g_l^{B(1,1)}$ in equation (3.17) contain the squared derivatives $j_l'^2(kp)$ as factor,

$$\begin{aligned} g_l^{A(1,1)} &= ak^{\mu_1} \mathrm{e}^{-\alpha_1 k^2 - \beta_1 k} j_l'^2(kp) \left[1 - \mathrm{Re}(\mathrm{e}^{-\mathrm{i}\omega k}) \cos\theta_0 - \mathrm{Im}(\mathrm{e}^{-\mathrm{i}\omega k}) \sin\theta_0\right], \\ g_l^{B(1,1)} &= bk^{\mu_2} \mathrm{e}^{-\alpha_2 k^2 - \beta_2 k} j_l'^2(kp) \left[1 + \mathrm{Re}(\mathrm{e}^{-\mathrm{i}\omega k}) \cos\theta_0 + \mathrm{Im}(\mathrm{e}^{-\mathrm{i}\omega k}) \sin\theta_0\right]. \end{aligned} \tag{3.19}$$

The contributions $g_l^{A(0,1)}$ and $g_l^{B(0,1)}$ to the spectral functions (3.17) stem from the mixed terms $j_l(kp) j_l'(kp)$ in equation (3.11),

$$\begin{aligned} g_l^{A(0,1)} &= ak^{\mu_1} \mathrm{e}^{-\alpha_1 k^2 - \beta_1 k} j_l(kp) j_l'(kp) \\ &\quad \times \Big[- \mathrm{Im}(\mathrm{e}^{-\mathrm{i}(\omega+\omega_0)k}) \cos(\theta_0 + \varphi_0) + \mathrm{Re}(\mathrm{e}^{-\mathrm{i}(\omega+\omega_0)k}) \sin(\theta_0 + \varphi_0) \\ &\quad - \mathrm{Im}(\mathrm{e}^{-\mathrm{i}(\omega-\omega_0)k}) \cos(\theta_0 - \varphi_0) + \mathrm{Re}(\mathrm{e}^{-\mathrm{i}(\omega-\omega_0)k}) \sin(\theta_0 - \varphi_0) \Big] \end{aligned} \tag{3.20}$$

and

$$\begin{aligned} g_l^{B(0,1)} &= bk^{\mu_2} \mathrm{e}^{-\alpha_2 k^2 - \beta_2 k} j_l(kp) j_l'(kp) \\ &\quad \times \Big[\mathrm{Im}(\mathrm{e}^{-\mathrm{i}(\omega+\omega_0)k}) \cos(\theta_0 + \varphi_0) - \mathrm{Re}(\mathrm{e}^{-\mathrm{i}(\omega+\omega_0)k}) \sin(\theta_0 + \varphi_0) \\ &\quad + \mathrm{Im}(\mathrm{e}^{-\mathrm{i}(\omega-\omega_0)k}) \cos(\theta_0 - \varphi_0) - \mathrm{Re}(\mathrm{e}^{-\mathrm{i}(\omega-\omega_0)k}) \sin(\theta_0 - \varphi_0) \Big]. \end{aligned} \tag{3.21}$$

The multipole coefficients $C_l^{A,B}(p)$ in equation (3.13) are obtained by integration of the spectral functions (3.17)–(3.21), cf. Section 4. We have written the harmonics depending on the spectral variable k as real and imaginary parts of exponentials to facilitate this integration.

4 RECONSTRUCTION OF THE CMB TEMPERATURE POWER SPECTRUM

4.1 Assembling the multipole coefficients: integrated spectral functions

We start with the Bessel integral

$$D_{\rm ssB}(l,\,p;\mu,\alpha,\beta,\omega)=\int_0^\infty k^{\mu+2}{\rm e}^{-\alpha k^2-(\beta+{\rm i}\omega)k}\,j_l^2(pk){\rm d}k, \tag{4.1}$$

with real exponents $\alpha\geq 0$, β, ω and μ. If $\alpha=0$, we assume a positive exponent β. The multipole component $C_l^{(N=1)}(p)$ in equation (3.13), generated by density $P(k)$ in equation (3.14), reads

$$C_l^{(N=1)}(p)=\sum_i C_l^{(1,i)}(p),\quad C_l^{(1,i)}(p)=\frac{2}{\pi}a_{0,i}\,D_{\rm ssB}(l,\,p;\mu_{0,i},\alpha_{0,i},\beta_{0,i},0). \tag{4.2}$$

Occasionally, we will indicate the parameter dependence, $C_l^{(1,i)}(p;a_{0,i},\mu_{0,i},\alpha_{0,i},\beta_{0,i})$. In the figures, we label the contribution of the components $C_l^{(1,i)}(p)$ to the total multipole coefficients C_l by P_i. The low-l region of the CMB temperature power spectrum, the main peak, as well as the crossover to the modulated decaying slope is an additive combination of eight Gaussian peaks, cf. Figs 1 and 2, so that the summation index in equation (4.2) runs from $i=1$ to 8, cf. Table 1. A detailed description of the multipole fit in the Gaussian regime, in particular of the fitting parameters of the Gaussian peaks recorded in Table 1, is given in Section 5.1, after having discussed the scaling relations and the scale-invariant limit of the Gaussian and oscillatory multipole components in Section 4.2.

As for the oscillatory multipole component $C_l^{(N=2)}(p)$ in equation (3.13), generated by the Hermitian kernel (3.5), we replace the squared spherical Bessel function in integral (4.1) by a product of derivatives,

$$D_{\rm ssB}^{(m,n)}(l,\,p;\mu,\alpha,\beta,\omega)=\int_0^\infty k^{\mu+2}{\rm e}^{-\alpha k^2-(\beta+{\rm i}\omega)k}\,j_l^{(m)}(pk)\,j_l^{(n)}(pk){\rm d}k, \tag{4.3}$$

so that $D_{\rm ssB}^{(0,0)}=D_{\rm ssB}$. These integrals are convergent for $\mu>-3$ and Re $\alpha>0$ or Re $\alpha=0$ and $\beta>0$. The coefficients $C_l^{(N=2)}$ can be split, according to equations (3.13) and (3.17)–(3.21), as

$$\begin{aligned}
&C_l^{(N=2)}(p)=C_l^A(p)+C_l^B(p),\\
&C_l^A(p)=C_l^{A(0,0)}+pC_l^{A(0,1)}+p^2C_l^{A(1,1)},\\
&C_l^B(p)=C_l^{B(0,0)}+pC_l^{B(0,1)}+p^2C_l^{B(1,1)}.
\end{aligned} \tag{4.4}$$

The superscript (0,0) indicates the j_l^2-dependent multipole component (stemming from the spectral functions $g_l^{A(0,0)}$ and $g_l^{B(0,0)}$ in equation 3.18), calculated as linear combination of the averages $D_{\rm ssB}^{(0,0)}$ in equation (4.3):

$$\begin{aligned}
C_l^{A(0,0)}=\frac{2}{\pi}a\Big[&D_{\rm ssB}^{(0,0)}(l,\,p;\mu_1,\alpha_1,\beta_1,0)+\cos\theta_0{\rm Re}D_{\rm ssB}^{(0,0)}(l,\,p;\mu_1,\alpha_1,\beta_1,\omega)\\
&+\sin\theta_0{\rm Im}D_{\rm ssB}^{(0,0)}(l,\,p;\mu_1,\alpha_1,\beta_1,\omega)\Big]
\end{aligned} \tag{4.5}$$

and

$$\begin{aligned}
C_l^{B(0,0)}=\frac{2}{\pi}b[&D_{\rm ssB}^{(0,0)}(l,\,p;\mu_2,\alpha_2,\beta_2,0)-\cos\theta_0{\rm Re}D_{\rm ssB}^{(0,0)}(l,\,p;\mu_2,\alpha_2,\beta_2,\omega)\\
&-\sin\theta_0{\rm Im}D_{\rm ssB}^{(0,0)}(l,\,p;\mu_2,\alpha_2,\beta_2,\omega)].
\end{aligned} \tag{4.6}$$

The parameter dependence of these moments is $C_l^{A(0,0)}(p;a,\mu_1,\alpha_1,\beta_1;\omega,\theta_0)$ and $C_l^{B(0,0)}(p;b,\mu_2,\alpha_2,\beta_2;\omega,\theta_0)$. The frequency ω and the angle θ_0 stem from the parametrization (3.15) of the matrix kernel (3.5). We also note that $\mu_{1,2}>-3$ is a requirement for the coefficients $C_{l=0}^{A(0,0)}$ and $C_{l=0}^{B(0,0)}$ to be convergent, and similarly for $C_{l=0}^{(1,i)}$ in equation (4.2), where $\mu_{0,i}>-3$ is required. The zeroth multipole moment $C_{l=0}$

Table 1. Parameters determining the Gaussian peaks P_i, $i=1,\ldots,8$, depicted in Figs 1, 2 and 6–11. Each peak P_i represents a multipole component $C_l^{(1,i)}(p=1;a_{0,i},\mu_{0,i}=0,\alpha_{0,i},\beta_{0,i})$, cf. (5.2), depending on the listed fitting parameters. The Gaussian moments $C_l^{(1,i)}$ are obtained by averaging squared spherical Bessel functions with Gaussian densities $\propto{\rm e}^{-\alpha k^2-\beta k}$, cf. (3.14), (4.1) and Section 5.1.

i	$a_{0,i}$	$\alpha_{0,i}$	$\beta_{0,i}$	$r_{0,i}=-\alpha_{0,i}/\beta_{0,i}$
1	2.5×10^{2}	6.25×10^{-2}	-0.25	0.25
2	1.5	1.47×10^{-2}	-0.3	4.9×10^{-2}
3	5.0×10^{-5}	7.0×10^{-3}	-0.5	1.4×10^{-2}
4	2.1×10^{-2}	6.6×10^{-4}	-0.06	1.1×10^{-2}
5	3.6×10^{-5}	4.5×10^{-4}	-0.1	4.5×10^{-3}
6	3.05×10^{-3}	6.26×10^{-5}	-0.02	3.13×10^{-3}
7	1.0×10^{-16}	1.067×10^{-4}	-0.11	9.7×10^{-4}
8	9.5×10^{-19}	5.04×10^{-5}	-0.08	6.3×10^{-4}

of the CMB temperature fit depicted in the figures is safely finite (and positive), but does not show due to the $l(l+1)$ normalization of the moments. A preferable though less customary normalization of the C_l plots is $(l+1/2)^2$.

The superscript (1,1) in equation (4.4) indicates the $j_l'^2$-dependent contribution to the multipole moments, defined by $g_l^{A(1,1)}$ and $g_l^{B(1,1)}$ in equation (3.19), and calculated by means of the integrals $D_{\mathrm{ssB}}^{(1,1)}$ in equation (4.3):

$$C_l^{A(1,1)} = \frac{2}{\pi} a \Big[D_{\mathrm{ssB}}^{(1,1)}(l,\, p; \mu_1, \alpha_1, \beta_1, 0) - \cos\theta_0 \mathrm{Re} D_{\mathrm{ssB}}^{(1,1)}(l,\, p; \mu_1, \alpha_1, \beta_1, \omega) - \sin\theta_0 \mathrm{Im} D_{\mathrm{ssB}}^{(1,1)}(l,\, p; \mu_1, \alpha_1, \beta_1, \omega) \Big] \tag{4.7}$$

and

$$C_l^{B(1,1)} = \frac{2}{\pi} b \Big[D_{\mathrm{ssB}}^{(1,1)}(l,\, p; \mu_2, \alpha_2, \beta_2, 0) + \cos\theta_0 \mathrm{Re} D_{\mathrm{ssB}}^{(1,1)}(l,\, p; \mu_2, \alpha_2, \beta_2, \omega) + \sin\theta_0 \mathrm{Im} D_{\mathrm{ssB}}^{(1,1)}(l,\, p; \mu_2, \alpha_2, \beta_2, \omega) \Big]. \tag{4.8}$$

The parameter dependence is the same as of $C_l^{A(0,0)}$ and $C_l^{B(0,0)}$, cf. the text after equation (4.6).

The superscript (0,1) in equation (4.4) labels the multipole contribution of the mixed coefficients $j_l j_l'$, stemming from $g_l^{A(0,1)}$ in equation (3.20) and $g_l^{B(0,1)}$ in equation (3.21). We find, by means of the integrals $D_{\mathrm{ssB}}^{(0,1)}$ in equation (4.3),

$$C_l^{A(0,1)} = \frac{2}{\pi} a \Big[-\cos(\theta_0+\varphi_0) \mathrm{Im} D_{\mathrm{ssB}}^{(0,1)}(l,\, p; \mu_1, \alpha_1, \beta_1, \omega+\omega_0) + \sin(\theta_0+\varphi_0) \mathrm{Re} D_{\mathrm{ssB}}^{(0,1)}(l,\, p; \mu_1, \alpha_1, \beta_1, \omega+\omega_0) - \cos(\theta_0-\varphi_0) \mathrm{Im} D_{\mathrm{ssB}}^{(0,1)}(l,\, p; \mu_1, \alpha_1, \beta_1, \omega-\omega_0) + \sin(\theta_0-\varphi_0) \mathrm{Re} D_{\mathrm{ssB}}^{(0,1)}(l,\, p; \mu_1, \alpha_1, \beta_1, \omega-\omega_0) \Big] \tag{4.9}$$

and

$$C_l^{B(0,1)} = \frac{2}{\pi} b \Big[\cos(\theta_0+\varphi_0) \mathrm{Im} D_{\mathrm{ssB}}^{(0,1)}(l,\, p; \mu_2, \alpha_2, \beta_2, \omega+\omega_0) - \sin(\theta_0+\varphi_0) \mathrm{Re} D_{\mathrm{ssB}}^{(0,1)}(l,\, p; \mu_2, \alpha_2, \beta_2, \omega+\omega_0) + \cos(\theta_0-\varphi_0) \mathrm{Im} D_{\mathrm{ssB}}^{(0,1)}(l,\, p; \mu_2, \alpha_2, \beta_2, \omega-\omega_0) - \sin(\theta_0-\varphi_0) \mathrm{Re} D_{\mathrm{ssB}}^{(0,1)}(l,\, p; \mu_2, \alpha_2, \beta_2, \omega-\omega_0) \Big]. \tag{4.10}$$

The angles θ_0 and φ_0 and the frequencies ω and ω_0 are arbitrary constants, fitting parameters in the angular parametrization (3.15) of the matrix kernel. If we put $\omega_0 = 0$ and $\varphi_0 = \pi/2$, the coefficients $C_l^{A(0,1)}$ and $C_l^{B(0,1)}$ vanish, cf. the text after equation (3.10). Otherwise, their parameter dependence is $C_l^{A(0,1)}(p; a, \mu_1, \alpha_1, \beta_1; \omega, \theta_0, \omega_0, \varphi_0)$ and $C_l^{B(0,1)}(p; b, \mu_2, \alpha_2, \beta_2; \omega, \theta_0, \omega_0, \varphi_0)$, and the same holds for the total coefficients $C_l^A(p)$ and $C_l^B(p)$ in equation (4.4). As in equation (4.2), we may perform a summation over a set of 2×2 matrices, cf. (3.12),

$$\begin{aligned} C_l^{(N=2)}(p) &= \sum_i C_l^{(2,i)}(p), \quad C_l^{(2,i)}(p) = C_l^{A,i}(p) + C_l^{B,i}(p), \\ C_l^{A,i}(p) &:= C_l^A(p; a_i, \mu_{1,i}, \alpha_{1,i}, \beta_{1,i}; \omega_i, \theta_{0,i}, \omega_{0,i}, \varphi_{0,i}), \\ C_l^{B,i}(p) &:= C_l^B(p; b_i, \mu_{2,i}, \alpha_{2,i}, \beta_{2,i}; \omega_i, \theta_{0,i}, \omega_{0,i}, \varphi_{0,i}). \end{aligned} \tag{4.11}$$

The index i labels the parameter sets defining the two-dimensional matrices, cf. (3.5), (3.15) and (3.16), and each component function is compiled as stated in equations (4.4)–(4.10). In the CMB temperature fit, we put $\theta_{0,i} = \omega_{0,i} = \varphi_{0,i} = 0$ as well as $\alpha_{1,i} = \alpha_{2,i} = 0$ from the outset, so that the Bessel derivatives in equation (4.3) are averaged with a power-law density with modulated exponential cut-off (Kummer distribution). In the figures, we use the shortcut K_i^a to label the multipole component $C_l^{A,i}(p)$ and K_i^b for $C_l^{B,i}(p)$, as well as K_i^{a+b} for their sum $C_l^{(2,i)}(p)$, cf. the dotted curves in Figs 3 and 4. The fit of the CMB power spectrum is performed with two two-dimensional matrices, which suffice to adequately reproduce the oscillatory and high-l regimes, so that the summation in equation (4.11) is over $i = 1, 2$, cf. Table 2. The multipole fit in these regimes and the fitting parameters in Table 2 are explained in Section 5.2.

The total multipole coefficients C_l are obtained by adding the contribution of the one- and two-dimensional matrix kernels in equations (4.2) and (4.11),

$$C_l(p) = C_l^{(N=1)}(p) + C_l^{(N=2)}(p). \tag{4.12}$$

Table 2. Parameters of the Kummer distributions generating the multipole components K_i^a, K_i^b and K_i^{a+b}, $i = 1, 2$, in Figs 3–5 and 8–13. In the figures, K_i^a stands for the oscillatory multipole component $C_l^{A,i}(p = 1; a_i, \mu_{1,i}, \alpha_{1,i} = 0, \beta_{1,i}; \omega_i, \theta_{0,i} = 0)$, K_i^b for $C_l^{B,i}(p = 1; b_i, \mu_{2,i}, \alpha_{2,i} = 0, \beta_{2,i}; \omega_i, \theta_{0,i} = 0)$ and K_i^{a+b} for $C_l^{A,i} + C_l^{B,i}$, cf. (5.4). The $C_l^{A,i}$ and $C_l^{B,i}$ moments are linear combinations of squared spherical Bessel functions averaged with Kummer distributions $\propto k^\mu \mathrm{e}^{-(\beta+\mathrm{i}\omega)k}$ (power laws with modulated exponential cut-off), cf. Section 5.2. The fitting parameters of K_1^a and K_1^b are listed in the first row, and of K_2^a in the second.

i	a_i	$\mu_{1,i}$	$\beta_{1,i}$	b_i	$\mu_{2,i}$	$\beta_{2,i}$	ω_i
1	2.6×10^{-6}	1	4.6×10^{-3}	5.4×10^{-5}	0	2.3×10^{-3}	2.15×10^{-2}
2	6.6×10^{-13}	1	2.1×10^{-4}	0	–	–	0

The component $C_l^{(N=1)}(p)$ is a Gaussian average which dominates the low-l regime including the main peak, cf. the text after equation (4.2). The oscillatory component $C_l^{(N=2)}(p)$ generated by Kummer distributions reproduces the decaying modulated slope and the subsequent power-law ascent with exponential cut-off, cf. Figs 4 and 5. The crossover between the Gaussian main peak and the modulated slope consists of two secondary peaks of nearly equal height, to which the Gaussian and oscillatory multipole components in equation (4.12) contribute in equal measure, cf. Figs 9–11.

4.2 Scaling relations for the multipole moments

The Bessel integrals in equations (4.1) and (4.3) satisfy the scaling relation

$$D_{\rm ssB}^{(m,n)}(l,\,p;\mu,\alpha,\beta,\omega)=p^{-\mu-3}D_{\rm ssB}^{(m,n)}(l,\,1;\mu,\alpha/p^2,\beta/p,\omega/p). \tag{4.13}$$

Applying this to the Gaussian multipole components $C_l^{(1,i)}(p)$ in equation (4.2), we find

$$C_l^{(1,i)}(p;a_{0,i},\mu_{0,i},\alpha_{0,i},\beta_{0,i})=C_l^{(1,i)}(1;\tilde a_{0,i},\mu_{0,i},\tilde\alpha_{0,i},\tilde\beta_{0,i}), \tag{4.14}$$

where the parameter p has been scaled into the arguments

$$\tilde a_{0,i}=a_{0,i}/p^{\mu_{0,i}+3},\quad \tilde\alpha_{0,i}=\alpha_{0,i}/p^2,\quad \tilde\beta_{0,i}=\beta_{0,i}/p. \tag{4.15}$$

In particular, the scale factor $p^{-\mu\ -3}$ in equation (4.13) is absorbed by the indicated rescaling of the amplitude $a_{0,i}$ of the $C_l^{(1,i)}$, cf. (4.2). Thus, the p dependence of the Gaussian coefficients $C_l^{(1,i)}$ can be completely absorbed in the fitting parameters, resulting in scale invariance. In effect, we can put $p=1$ and use $C_l^{(1,i)}(1;a_{0,i},\mu_{0,i},\alpha_{0,i},\beta_{0,i})$ in the CMB temperature fit, with the indicated variables as independent fitting parameters, cf. Table 1.

We turn to the p scaling of the oscillatory multipole moments in equations (4.4) and (4.11), generated by the Hermitian kernel (3.5). The component functions $C_l^{A(0,0)}$ and $C_l^{B(0,0)}$ in equations (4.5) and (4.6) are scale invariant,

$$\begin{aligned}C_l^{A(0,0)}(p;a,\mu_1,\alpha_1,\beta_1;\omega,\theta_0)&=C_l^{A(0,0)}(1;\tilde a,\mu_1,\tilde\alpha_1,\tilde\beta_1;\tilde\omega,\theta_0),\\ C_l^{B(0,0)}(p;b,\mu_2,\alpha_2,\beta_2;\omega,\theta_0)&=C_l^{B(0,0)}(1;\tilde b,\mu_2,\tilde\alpha_2,\tilde\beta_2;\tilde\omega,\theta_0),\end{aligned} \tag{4.16}$$

as we can absorb the scaling parameter p in the fitting parameters,

$$\tilde a=a/p^{\mu_1+3},\quad \tilde b=b/p^{\mu_2+3},\quad \tilde\alpha_{1,2}=\alpha_{1,2}/p^2,\quad \tilde\beta_{1,2}=\beta_{1,2}/p,\quad \tilde\omega=\omega/p. \tag{4.17}$$

The coefficients $C_l^{A(1,1)}$ and $C_l^{B(1,1)}$ in equations (4.7) and (4.8) scale like $C_l^{A(0,0)}$ and $C_l^{B(0,0)}$ in equation (4.16). The mixed components $C_l^{A(0,1)}$ and $C_l^{B(0,1)}$ in equations (4.9) and (4.10) are likewise scale invariant,

$$\begin{aligned}C_l^{A(0,1)}(p;a,\mu_1,\alpha_1,\beta_1;\omega,\theta_0,\omega_0,\varphi_0)&=C_l^{A(0,1)}(1;\tilde a,\mu_1,\tilde\alpha_1,\tilde\beta_1;\tilde\omega,\theta_0,\tilde\omega_0,\varphi_0),\\ C_l^{B(0,1)}(p;b,\mu_2,\alpha_2,\beta_2;\omega,\theta_0,\omega_0,\varphi_0)&=C_l^{B(0,1)}(1;\tilde b,\mu_2,\tilde\alpha_2,\tilde\beta_2;\tilde\omega,\theta_0,\tilde\omega_0,\varphi_0),\end{aligned} \tag{4.18}$$

with the rescaled parameters listed in equation (4.17) and $\tilde\omega_0=\omega_0/p$.

Thus, the coefficients $C_l^A(p)$ and $C_l^B(p)$ in equations (4.4) and (4.11) reduce to second-order polynomials in p if we use the rescaled parameters (4.17) and $\tilde\omega_0$ as independent fitting parameters:

$$\begin{aligned}C_l^A(p;a,\mu_1,\alpha_1,\beta_1;\omega,\theta_0,\omega_0,\varphi_0)&=C_l^{A(0,0)}(1;\tilde a,\mu_1,\tilde\alpha_1,\tilde\beta_1;\tilde\omega,\theta_0)\\ &+pC_l^{A(0,1)}(1;\tilde a,\mu_1,\tilde\alpha_1,\tilde\beta_1;\tilde\omega,\theta_0,\tilde\omega_0,\varphi_0)+p^2C_l^{A(1,1)}(1;\tilde a,\mu_1,\tilde\alpha_1,\tilde\beta_1;\tilde\omega,\theta_0)\end{aligned} \tag{4.19}$$

and

$$\begin{aligned}C_l^B(p;b,\mu_2,\alpha_2,\beta_2;\omega,\theta_0,\omega_0,\varphi_0)&=C_l^{B(0,0)}(1;\tilde b,\mu_2,\tilde\alpha_2,\tilde\beta_2;\tilde\omega,\theta_0)\\ &+pC_l^{B(0,1)}(1;\tilde b,\mu_2,\tilde\alpha_2,\tilde\beta_2;\tilde\omega,\theta_0,\tilde\omega_0,\varphi_0)+p^2C_l^{B(1,1)}(1;\tilde b,\mu_2,\tilde\alpha_2,\tilde\beta_2;\tilde\omega,\theta_0).\end{aligned} \tag{4.20}$$

In the Gaussian multipole components (4.14), the scale parameter p can be absorbed in the fitting parameters, as done in equation (4.15). In contrast, in the oscillatory components $C_l^{(2,i)}=C_l^{A,i}+C_l^{B,i}$ compiled in equations (4.11), (4.19) and (4.20), there remains an explicit p dependence breaking the scale invariance. The scale parameter p enters as an additional fitting parameter, as a weight factor determining the contribution of the Bessel products j_l^2, j_lj_l' and $j_l'^2$ (weighted by 1, p and p^2, respectively) to the multipole moments. There is no other p dependence, as the rescaled variables indicated by a tilde in equations (4.19) and (4.20) are independent fitting parameters. Scale invariance is attained in the limit $p\to 0$, where the coefficients C_l^A and C_l^B coincide with $C_l^{A(0,0)}(1;\tilde a,\mu_1,\tilde\alpha_1,\tilde\beta_1;\tilde\omega,\theta_0)$ and $C_l^{B(0,0)}(1;\tilde b,\mu_2,\tilde\alpha_2,\tilde\beta_2;\tilde\omega,\theta_0)$, respectively. In effect, this means to discard the linear and quadratic p terms in equation (4.4) (which give the multipole contributions of the j_lj_l' and $j_l'^2$ products), and to put $p=1$ in the explicit expressions for $C_l^{A(0,0)}$ and $C_l^{B(0,0)}$ in equations (4.5) and (4.6). The rescaled variables in $C_l^{A(0,0)}$ and $C_l^{B(0,0)}$ can be renamed to the original ones, cf. (4.17), to arrive at

$$C_l^A=C_l^{A(0,0)}(1;a,\mu_1,\alpha_1,\beta_1;\omega,\theta_0),\quad C_l^B=C_l^{B(0,0)}(1;b,\mu_2,\alpha_2,\beta_2;\omega,\theta_0). \tag{4.21}$$

The multipole components (4.19) and (4.20) thus reduce to (4.21) in the scale-invariant limit $p=0$ adopted in the CMB temperature power fit. The fitting parameters indicated as arguments in (4.21) are listed in Table 2.

5 MULTIPOLE FINE STRUCTURE OF CMB TEMPERATURE FLUCTUATIONS

5.1 Gaussian multipole moments in the low-*l* region

To summarize, the CMB temperature multipole moments,

$$C_l = C_l^{(N=1)} + C_l^{(N=2)}, \tag{5.1}$$

plotted in Figs 1–13, are assembled from Gaussian and oscillatory components. The Gaussian moments, cf. (4.14),

$$C_l^{(N=1)} = \sum_i C_l^{(1,i)}(p=1; a_{0,i}, \mu_{0,i}=0, \alpha_{0,i}, \beta_{0,i}), \tag{5.2}$$

consist of Gaussian averages $C_l^{(1,i)}$ defined by the Bessel integrals in equations (4.1) and (4.2). In the figures, the plots of the individual components $C_l^{(1,i)}$, $i = 1, \ldots, 8$, are labelled by P_i, which stands for the Gaussian density (3.14) generating the respective coefficients $C_l^{(1,i)}$. In equation (5.2), the power-law exponents $\mu_{0,i}$ have been put to zero from the outset; the remaining fitting parameters $\alpha_{0,i}$, $\beta_{0,i}$ and $a_{0,i}$ determining the location, width and amplitude of the peaks $P_{i=1,\ldots,8}$ are listed in Table 1.

The peaks labelled P_i in the figures (dashed curves) are the l plots of the Gaussian multipole components $C_l^{(1,i)} = (2/\pi) a_{0,i} D_{\mathrm{ssB}}(l, 1; 0, \alpha_{0,i}, \beta_{0,i}, 0)$, cf. (4.2), where D_{ssB} is the Bessel integral (4.1). As a rule of thumb, the ratio $r_{0,i} = -\alpha_{0,i}/\beta_{0,i}$ listed in Table 1 determines the location of the peak P_i; a smaller $r_{0,i}$ shifts the peak to the right, towards higher l values. The negative exponent $\beta_{0,i}$ determines the width of the peak, a smaller $|\beta_{0,i}|$ resulting in a larger width. These qualitative features of the averages (4.1) hold particularly well for peaks at moderate and high l, such as P_7 and P_8 in the first transitional regime, cf. Fig. 10; the high-l asymptotics of the Bessel integrals in equations (4.1) and (4.3) and their numerical evaluation will be discussed elsewhere. The Gaussian component (5.2) dominates the CMB temperature fit at low l, up to about $l \sim 100$, cf. Figs 6 and 7. In this regime, the fit C_l is obtained by adding the Gaussian peaks P_i and a tiny admixture of the oscillatory component $C_l^{(N=2)}$ in equation (5.1), emerging at the lower edge of Fig. 6 as dotted curve K_1^{a+b}. The main peak shown in Figs 8 and 9 is essentially generated by the Gaussian peak P_6, with admixtures of smaller adjacent Gaussian peaks and the mentioned oscillatory component $K_1^{a+b} = K_1^a + K_1^b$ (discussed in Section 5.2), which becomes more dominant with increasing l. The main peak covers the multipole region $100 \leq l \leq 400$.

5.2 Oscillatory multipole spectrum generated by Kummer distributions in the transitional and high-*l* regimes

The oscillatory moments $C_l^{(N=2)}$ in equation (5.1) are compiled as, cf. (4.11) and (4.21),

$$C_l^{(N=2)} = \sum_i C_l^{(2,i)}, \quad C_l^{(2,i)} = C_l^{A,i} + C_l^{B,i}, \tag{5.3}$$

where we use the shortcuts

$$\begin{aligned} C_l^{A,i} &= C_l^{A(0,0)}(p=1; a_i, \mu_{1,i}, \alpha_{1,i}=0, \beta_{1,i}; \omega_i, \theta_{0,i}=0), \\ C_l^{B,i} &= C_l^{B(0,0)}(p=1; b_i, \mu_{2,i}, \alpha_{2,i}=0, \beta_{2,i}; \omega_i, \theta_{0,i}=0), \end{aligned} \tag{5.4}$$

for the component functions $C_l^{A(0,0)}$ and $C_l^{B(0,0)}$, which are explicitly stated in equations (4.5) and (4.6) as linear combinations of the Bessel averages (4.3). In equation (5.4), we have put the exponents $\alpha_{1,i}$ and $\alpha_{2,i}$ to zero from the outset, which means to drop the quadratic term in the exponentials in equation (4.3). We have also equated the angle $\theta_{0,i}$ to zero, which appears in the angular parametrization (3.15) of the Hermitian spectral matrices generating the oscillatory moments. The CMB temperature fit in Figs 1–13 is performed with the total moments C_l in equation (5.1), obtained by adding the Gaussian moments (5.2) specified in Table 1 to the oscillatory moments listed in equations (5.3) and (5.4) and Table 2.

The decaying modulated slope in Figs 11 and 12 and the subsequent power-law rise of C_l in Fig. 13 are generated by the multipole component (5.3); the Gaussian peaks (5.2) do not affect multipoles beyond $l \sim 1000$. The plots of the individual components $C_l^{A,i=1,2}$ in equation (5.4) are labelled by $K_{i=1,2}^a$ in the figures, the plot of $C_l^{B,1}$ by K_1^b and the plot of the sum $C_l^{(2,i=1)}$ in equation (5.3) by K_1^{a+b}. The component $C_l^{A,2}$ (labelled K_2^a) suffices to model the high-l regime, so that we have put $C_l^{B,2} = 0$. K_1^a, K_1^b and K_2^a stand for Kummer distributions $k^\mu \mathrm{e}^{-(\beta+\mathrm{i}\omega)k}$ in the Bessel averages (4.3) defining the moments $C_l^{A,1}$, $C_l^{B,1}$ and $C_l^{A,2}$ in equation (5.4), cf. Table 2.

In the first row of Table 2, we have listed the fitting parameters of the moments $C_l^{A,1}$ and $C_l^{B,1}$, which constitute the oscillatory multipole component generating the decaying intermediate-l slope in Figs 11 and 12. In the interval $1000 \leq l \leq 2500$, the multipole fit essentially consists of these two components, $C_l \sim C_l^{A,1} + C_l^{B,1}$, whose plots (dotted curves) are labelled K_1^a and K_1^b in the figures. The moments C_l are obtained by adding these two curves, cf. Figs 11 and 12; the contributions of the Gaussian peak P_8 and of the ascending slope K_2^a (both indicated at the lower edge of Fig. 12) are negligible in this interval. The second row of Table 2 contains the fitting parameters of the moments $C_l^{A,2}$ (depicted as dotted curve K_2^a in Figs 12 and 13), which dominate the fit above $l \sim 4000$, $C_l \sim C_l^{A,2}$. This component generates the extended non-Gaussian peak at $l \approx 15\,400$ in Fig. 5.

In Section 5.1, we have studied the Gaussian regime $0 \leq l \leq 400$, cf. Figs 6–9. In this section, we discuss the intermediate oscillatory regime, the interval $1000 \leq l \leq 2500$ containing the modulated decaying slope of C_l, cf. Figs 11 and 12, as well as the high-l regime above $l \sim 4000$, cf. Fig. 13. There are two transitional regimes. The first, $400 \leq l \leq 1000$, is the crossover region from the Gaussian to the oscillatory regime depicted in Figs 8–11. The crossover consists of two secondary peaks of nearly the same height following the main peak. These peaks

are the result of pronounced modulations in the oscillatory component (comprising the moments $C_l^{A,1}$ and $C_l^{B,1}$ discussed above and depicted as dotted curves K_1^a and K_1^b) and of two Gaussian peaks P_7 and P_8 located in this transitional region. The fit in the crossover interval $400 \leq l \leq 1000$ is thus obtained as $C_l \sim P_7 + P_8 + K_1^a + K_1^b$, with a small admixture from the main peak P_6, cf. Fig. 10. The second transitional regime is the interval $2500 \leq l \leq 4000$, cf. Fig. 12, joining the oscillatory multipole component $C_l^{A,1} + C_l^{B,1}$ to the ascending power-law slope of the high-l component $C_l^{A,2}$. The fit $C_l \sim K_1^{a+b} + K_2^a$ in this crossover region is obtained by adding the exponentially damped tail $K_1^{a+b} = K_1^a + K_1^b$ to the emerging rising slope K_2^a, cf. Figs 12 and 13, the latter dominating the multipole spectrum above $l \sim 4000$.

6 OUTLOOK: MULTICOMPONENT SPHERICAL RANDOM FIELDS

We consider $T(\boldsymbol{p})$ as a component of a multicomponent scalar field $\psi_i(\boldsymbol{p})$ on the sphere, where the index $i = T, E, B, \ldots$ labels, for instance, temperature, E and B polarization, circular polarization if detectable, an angular galaxy distribution, etc. The temperature field $T(\boldsymbol{p})$ reads in this notation $\psi_T(\boldsymbol{p})$. The counterpart to the Green function $\langle T(\boldsymbol{p})T(\boldsymbol{p}')\rangle$ in equation (2.27) is

$$G_{ij}(\boldsymbol{p}_0, \boldsymbol{p}_0'; p) = \langle \psi_i(\boldsymbol{p})\psi_j(\boldsymbol{p}')\rangle = \frac{1}{4\pi}\sum_{l=0}^{\infty}(2l+1)C_{ij;l}(p)P_l(\boldsymbol{p}_0\boldsymbol{p}_0'). \tag{6.1}$$

The multipole coefficients $C_{ij;l}$ are symmetric in i and j, assembled by averaging squared spherical Bessel functions with Gaussian power laws and Kummer distributions as explained in Sections 3 and 4. The Hermitian spectral kernels defining the off-diagonal elements need not be positive definite, so that the diagonal matrices in the decomposition (3.3) and (B1) can have negative coefficients, also see the text after equation (3.16). The inverse $G_{ij}^{-1}(\boldsymbol{p}_0, \boldsymbol{p}_0'; p)$ is defined by the same series with the real symmetric multipole coefficients $C_{ij;l}$ replaced by the inverse matrices $C_{ij;l}^{-1}(p)$. By making use of the orthogonality relation (2.6) of Legendre polynomials and the series representation (2.13) of the delta function on the unit sphere, we find

$$\sum_{k=T,E,B,\ldots}\int G_{ik}(\boldsymbol{p}_0, \boldsymbol{n}; p)G_{kj}^{-1}(\boldsymbol{n}, \boldsymbol{p}_0'; p)\mathrm{d}\Omega_{\boldsymbol{n}} = \delta_{ij}\delta_\Omega(\boldsymbol{p}_0, \boldsymbol{p}_0'). \tag{6.2}$$

The kernels $G_{ij}^{\pm1}(\boldsymbol{p}_0, \boldsymbol{p}_0'; p)$ are real and symmetric, depending only on $\boldsymbol{p}_0\boldsymbol{p}_0' = \cos\theta$ and the scale parameter p. Due to the assumed isotropy, it suffices to expand the Green function in Legendre polynomials rather than in products of spherical harmonics. Isotropy is crucial if the CMB rest frame is to define an absolute frame of reference (Tomaschitz 2012).

The matrices $C_{ij;l}(p)$ can be regarded as positive definite, as the positive $C_{TT;l}(p)$ component usually overpowers all others, so that the inverse correlation function (6.1) is a Gaussian kernel. [Even if the $C_{ij;l}$ are not invertible, one can try the characteristic functional (6.6) as a starting point, instead of the Gaussian density (6.5), to generate n-point correlations.] As we will only use unit vectors in this section, we drop the zero subscripts as well as the scale parameter as argument, writing $G_{ij}^{\pm1}(\boldsymbol{p}, \boldsymbol{p}')$ or $\langle\psi_i(\boldsymbol{p})\psi_j(\boldsymbol{p}')\rangle$ for the Green function (6.1) and its inverse on the unit sphere $|\boldsymbol{p}| = |\boldsymbol{p}'| = 1$. Spherical integrations are denoted by the solid-angle element $\mathrm{d}\Omega_p$, and the real random variables by $\psi_i(\boldsymbol{p})$. The multipole expansion (6.1) can be inverted by way of the orthogonality relation (2.6) and $P_l(1) = 1$,

$$C_{ij;l} = \frac{1}{4\pi}\iint\langle\psi_i(\boldsymbol{p}_1)\psi_j(\boldsymbol{p}_2)\rangle P_l(\boldsymbol{p}_1\boldsymbol{p}_2)\mathrm{d}\Omega_{p_1}\mathrm{d}\Omega_{p_2}. \tag{6.3}$$

The second solid-angle integration has been added for symmetry reasons.

The observationally determined Green function is found by specifying the multipole coefficients in equations (6.1) and (6.3) as $C_{ij;l} = C_{ij;l}^{\mathrm{map}}$, where $C_{ij;l}^{\mathrm{map}}$ are coefficients extracted from the two-dimensional CMB maps, by replacing the average $\langle\psi_i(\boldsymbol{p}_1)\psi_j(\boldsymbol{p}_2)\rangle$ in equation (6.3) by the product $\psi_i(\boldsymbol{p}_1)\psi_j(\boldsymbol{p}_2)$ of the measured field components. We may substitute the integral representation of the coefficients $C_{ij;l}^{\mathrm{map}}$ (i.e. equation 6.3 without angle brackets) into the Legendre series (6.1), interchange integration and summation, and use the completeness relation (A4) of the Legendre polynomials. In this way, we arrive at an integral representation of the Green function equivalent to the Legendre series (6.1) (with $C_{ij;l}^{\mathrm{map}}$ as coefficients),

$$G_{ij}(\boldsymbol{p}_0, \boldsymbol{p}_0') = \frac{1}{8\pi^2}\iint\psi_i(\boldsymbol{p}_1)\psi_j(\boldsymbol{p}_2)\delta(\boldsymbol{p}_1\boldsymbol{p}_2 - \boldsymbol{p}_0\boldsymbol{p}_0')\mathrm{d}\Omega_{p_1}\mathrm{d}\Omega_{p_2}. \tag{6.4}$$

In Section 4, we derived an analytic approximation to the temperature autocorrelation $G_{TT}(\boldsymbol{p}_0, \boldsymbol{p}_0')$ based on the observed field configuration $\psi_T(\boldsymbol{p})$, and found an integral approximation of the measured coefficients $C_{TT;l}^{\mathrm{map}}$ which is uniform in l, covering the multipole range depicted in the figures.

The inverse of the Green function (6.4) (identical to the Legendre series 6.1 with expansion coefficients $C_{ij;l}^{\mathrm{map}}$) is the kernel of a Gaussian density,

$$p[\psi] = \exp\left[-\frac{1}{2}\iint\psi_i(\boldsymbol{p})G_{ij}^{-1}(\boldsymbol{p}, \boldsymbol{p}')\psi_j(\boldsymbol{p}')\mathrm{d}\Omega_p\mathrm{d}\Omega_{p'}\right]. \tag{6.5}$$

The Fourier transform $\langle\exp[-\mathrm{i}\int\varphi_i(\boldsymbol{p})\psi_i(\boldsymbol{p})\mathrm{d}\Omega_p]\rangle$ of the normalized density reads

$$\hat{p}[\varphi] = \exp\left[-\frac{1}{2}\iint\varphi_i(\boldsymbol{p})G_{ij}(\boldsymbol{p}, \boldsymbol{p}')\varphi_j(\boldsymbol{p}')\mathrm{d}\Omega_p\mathrm{d}\Omega_{p'}\right], \tag{6.6}$$

obtained by introducing a new integration variable $\tilde{\psi}_i(\boldsymbol{p})$ in the Fourier integral via the shift $\psi_i(\boldsymbol{p}) = \tilde{\psi}_i(\boldsymbol{p}) - \mathrm{i}\int G_{ij}(\boldsymbol{p}, \boldsymbol{q})\varphi_j(\boldsymbol{q})\mathrm{d}\Omega_q$ and by employing identity (6.2). The n-point correlations are generated by multiple differentiation of $\hat{p}[\varphi]$, using functional derivatives on the

unit sphere, $\delta\varphi_i(\boldsymbol{p})/\delta\varphi_j(\boldsymbol{p}') = \delta_{ij}\delta_\Omega(\boldsymbol{p}, \boldsymbol{p}')$, with the spherical delta function δ_Ω. In this way, we find the Wick expansion of the four-point function,

$$\langle\psi_{i_1}(\boldsymbol{p}_1)\psi_{i_2}(\boldsymbol{p}_2)\psi_{i_3}(\boldsymbol{p}_3)\psi_{i_4}(\boldsymbol{p}_4)\rangle = \sigma_{12}\sigma_{34} + \sigma_{13}\sigma_{24} + \sigma_{14}\sigma_{32}, \tag{6.7}$$

in products of the Green functions $\sigma_{ab} = G_{i_a i_b}(\boldsymbol{p}_a, \boldsymbol{p}_b) = \langle\psi_{i_a}(\boldsymbol{p}_a)\psi_{i_b}(\boldsymbol{p}_b)\rangle$, $i_{a,b} = T, E, B, \ldots$. If there is an odd number of factors, the expectation value vanishes. The $2n$-point function is obtained by summing a product of n factors σ_{ab} over all unordered index pairs according to the pattern (6.7); there are $(2n)!/(n!2^n)$ summands.

We consider the Legendre-weighted average of the four-point correlation (6.7),

$$\left\langle C^{(4)}_{i_1,\ldots,i_4;lk}\right\rangle = \frac{1}{(4\pi)^2}\int\langle\psi_{i_1}(\boldsymbol{p}_1)\psi_{i_2}(\boldsymbol{p}_2)\psi_{i_3}(\boldsymbol{p}_3)\psi_{i_4}(\boldsymbol{p}_4)\rangle P_l(\boldsymbol{p}_1\boldsymbol{p}_2)P_k(\boldsymbol{p}_3\boldsymbol{p}_4)\mathrm{d}\Omega_{p_1}\mathrm{d}\Omega_{p_2}\mathrm{d}\Omega_{p_3}\mathrm{d}\Omega_{p_4}, \tag{6.8}$$

which can be evaluated as

$$\left\langle C^{(4)}_{i_1,\ldots,i_4;lk}\right\rangle = C_{i_1i_2;l}C_{i_3i_4;k} + \frac{\delta_{lk}}{2l+1}\left(C_{i_1i_3;l}C_{i_2i_4;l} + C_{i_1i_4;l}C_{i_2i_3;l}\right). \tag{6.9}$$

Here, we used equations (6.3), (6.7) and the series representation (6.1) as well as the integral

$$\int P_l(\boldsymbol{p}_1\boldsymbol{p}_2)P_k(\boldsymbol{p}_3\boldsymbol{p}_4)P_m(\boldsymbol{p}_1\boldsymbol{p}_3)P_n(\boldsymbol{p}_2\boldsymbol{p}_4)\mathrm{d}\Omega_{p_1}\mathrm{d}\Omega_{p_2}\mathrm{d}\Omega_{p_3}\mathrm{d}\Omega_{p_4} = \frac{(4\pi)^4}{(2l+1)^3}\delta_{lk}\delta_{lm}\delta_{kn}, \tag{6.10}$$

where the variables can be interchanged in pairs, $\boldsymbol{p}_i \leftrightarrow \boldsymbol{p}_j$. The integrations over the four unit spheres in equation (6.10) are readily done by repeated application of the orthogonality relation for Legendre polynomials in equation (2.6). Weighted higher order correlations such as $\langle C^{(6)}_{i_1,\ldots,i_6;lkm}\rangle$ are defined according to patterns (6.3) and (6.8), and can be expressed as linear combinations of products of multipole coefficients analogous to equation (6.9).

We rename the indices in equation (6.9) to $i_{1,2,3,4} = i, j, m, n$. The covariance matrix $\langle\Delta C_{ij;l}\Delta C_{mn;k}\rangle$, $\Delta C_{ij;l} = C^{\mathrm{map}}_{ij;l} - C_{ij;l}$, thus reads

$$\left\langle\Delta C_{ij;l}\Delta C_{mn;k}\right\rangle = \langle C^{(4)}_{ijmn;lk}\rangle - C_{ij;l}C_{mn;k} = \frac{\delta_{lk}}{2l+1}(C_{im;l}C_{jn;l} + C_{in;l}C_{jm;l}), \tag{6.11}$$

which gives the cosmic variance $\sigma^2_{ij;l} = \langle\Delta C_{ij;l}\Delta C_{ij;l}\rangle$. The angle brackets refer to the Gaussian functional (6.5) and can formally be imagined as ensemble average over multiple copies of the sky, with root mean squares $\sigma_{ij;l}$ quantifying the fluctuations of the coefficients $C_{ij;l}$. This ensemble interpretation is borrowed from statistical mechanics, but is less appealing here, as the ensemble and the average to which the $\sigma_{ij;l}$ refer are not realizable. The large error bars at low l, cf. Figs 6 and 7, are almost entirely due to cosmic variance (calculated via equation 6.11 with $C_{ij;l} = C^{\mathrm{map}}_{ij;l}$), as the measurement errors are very small at low l as compared to $\sigma_{ij;l}$ (Jarosik et al. 2011; Larson et al. 2011). The depicted error bars obscure the fine structure of the low-l power spectrum of the measured field configuration, the only accessible one of the envisaged ensemble. Here, we have found an analytic Green function for the temperature autocorrelation, which fits the power spectrum within the actual measurement errors (rather than within the error bars defined by the variance of a hypothetical ensemble average over independent universes).

By identifying the pairs $(i_a, \boldsymbol{p}_a)$ in the four-point function (6.7), one obtains contractions such as $\langle\psi^2_{i_1}(\boldsymbol{p}_1)\psi^2_{i_2}(\boldsymbol{p}_2)\rangle = \sigma_{11}\sigma_{22} + 2\sigma^2_{12}$, where σ_{11} and σ_{22} are constants and σ^2_{12} is the squared two-point function (6.1) depending on $\boldsymbol{p}_1\boldsymbol{p}_2 = \cos\theta$. Correlations on large angular scales, e.g. the weak temperature autocorrelation at $\theta \geq \pi/3$ (Bennett et al. 2011), are quantified by truncated angular averages such as $S_{ij}(\theta) = \int_\theta^\pi G^2_{ij}(\cos\theta)\sin\theta\mathrm{d}\theta$, which can be evaluated by means of the Legendre series (6.1) and the uniform analytic approximation of the multipole coefficients stated in Section 4.

7 CONCLUSION

We designed an analytic method to reconstruct correlation functions of spherical Gaussian random fields from measured power spectra. The isotropic correlations are defined by a Hermitian matrix kernel, composed of Gaussian power-law densities and Kummer distributions. We obtained a closed analytic expression for the CMB temperature autocorrelation function, fitted its kernel to the measured multipole spectrum and tested the quality of the fit in various intervals over an extended multipole range, cf. Figs 6–13. The multipole coefficients are obtained by averaging squared spherical Bessel functions with the matrix kernel of the Green function, cf. Section 3. In Tables 1 and 2, we list the fitting parameters of the distributions defining the spectral kernel. Once the kernel of the Green function is specified, so are all higher n-point correlations of the Gaussian random field.

The fine structure of the CMB temperature power spectrum in the low-l regime suggests that the Sachs–Wolfe 'plateau' precursory to the main peak is a superposition of overlapping Gaussian peaks, shown in Figs 6 and 7 as dashed curves. In contrast, the high-l power spectrum above $l \sim 1000$ consists of two non-Gaussian oscillatory components (depicted in Figs 9–13 as dotted curves $K_1^{a+b} = K_1^a + K_1^b$ and K_2^a) generated by Kummer distributions, cf. Table 2.

The fine structure of CMB power spectra can be hidden in compressed spectral plots as shown in Figs 1–5, which give no more than an overview of the basic features of the spectral map, and make it even difficult to identify the Gaussian and transitional peaks and to discern them from periodic modulations. The low-l regime up to $l \sim 400$ is composed of Gaussian peaks, cf. Figs 6 and 7. The two transitional peaks in the crossover region $400 \leq l \leq 1000$, cf. Figs 8 and 9, are mixtures of Gaussian peaks and large-amplitude modulations of the Kummer distributions. The intermediate and high-l multipole regimes in Figs 12 and 13 comprise a modulated decaying slope K_1^{a+b} and a rising power-law slope K_2^a stemming from the Kummer distributions in the spectral kernel of the correlation function.

Hermitian spectral matrices are an efficient analytic tool to reconstruct correlation functions of spherical Gaussian random fields from angular power spectra. Here, we studied the CMB temperature autocorrelation, based on a multipole spectrum measured up to $l \sim 10^4$, cf. Fig. 1. Other applications are CMB polarization correlations and temperature–polarization cross-correlations, or galaxy angular correlations. In all these cases, the multipole expansion of the spherical Green function is a Legendre series in zonal spherical harmonics due to isotropy, cf. Section 6, so that the correlation functions can be reconstructed from the measured (cross-)power spectra as described in Sections 3 and 4.

REFERENCES

Bennett C. L. et al., 2011, ApJS, 192, 17
Brown M. L. et al., 2009, ApJ, 705, 978
Das S. et al., 2011, ApJ, 729, 62
Jackson J. D., 1999, Classical Electrodynamics, 3rd edn. Wiley, New York
Jarosik N. et al., 2011, ApJS, 192, 14
Jeans J. H., 1923, Proc. R. Soc. A, 102, 554
Jones W. C. et al., 2006, ApJ, 647, 823
Keisler R. et al., 2011, ApJ, 743, 28
Landau L. D., Lifshitz E. M., 1991, Quantum Mechanics: Non-Relativistic Theory, 3rd edn. Pergamon, London
Larson D. et al., 2011, ApJS, 192, 16
Magnus W., Oberhettinger F., Soni R. P., 1966, Formulas and Theorems for the Special Functions of Mathematical Physics. Springer, New York
Nakamura K. et al., 2010, J. Phys. G, 37, 075021, http://pdg.lbl.gov
Newton R. G., 1982, Scattering Theory of Waves and Particles. Springer, New York
Olver F. W. J., Lozier D. W., Boisvert R. F., Clark C. W., 2010, NIST Handbook of Mathematical Functions. Cambridge Univ. Press, Cambridge, http://dlmf.nist.gov
Reichardt C. L. et al., 2009, ApJ, 694, 1200
Reichardt C. L. et al., 2012, ApJ, 755, 70
Sievers J. M. et al., 2009, preprint (arXiv:0901.4540)
Tomaschitz R., 2012, Europhys. Lett., 97, 39003

APPENDIX A: DELTA FUNCTION AND LEGENDRE EXPANSION ON THE UNIT SPHERE

The delta function $\delta_\Omega(\boldsymbol{n},\boldsymbol{n}')$ on the unit sphere $|\boldsymbol{n}| = 1$ can be defined by $\int f(\boldsymbol{n})\delta_\Omega(\boldsymbol{n},\boldsymbol{n}')\mathrm{d}\Omega_{\boldsymbol{n}} = f(\boldsymbol{n}')$, where $\mathrm{d}\Omega_{\boldsymbol{n}} = \sin\theta\mathrm{d}\theta\mathrm{d}\varphi$ is the solid-angle element with polar axis $\boldsymbol{n}$, and $f(\boldsymbol{n})$ is an arbitrary smooth and square-integrable function on the unit sphere. Thus, $\delta_\Omega(\boldsymbol{n},\boldsymbol{n}') = \delta(\varphi-\varphi')\delta(\cos\theta-\cos\theta')$, with $\delta(\cos\theta-\cos\theta') = \delta(\theta-\theta')/\sin\theta$, where the angles (θ,φ) and (θ',φ') are the polar coordinates of the unit vectors $\boldsymbol{n}$ and $\boldsymbol{n}'$.

Spherical harmonics $Y_{lm}(\theta,\varphi)$ are denoted by $Y_{lm}(\boldsymbol{n})$, where $\boldsymbol{n}(\theta,\varphi)$ is a unit vector in polar coordinates. The $Y_{lm}(\theta,\varphi)$, $l = 0, 1, 2\ldots$, $-l \le m \le l$, are complete on the unit sphere; their orthogonality and completeness relations (Olver et al. 2010) read in this notation

$$\int Y_{lm}(\boldsymbol{n})Y^*_{l'm'}(\boldsymbol{n})\mathrm{d}\Omega_{\boldsymbol{n}} = \delta_{ll'}\delta_{mm'}, \tag{A1}$$

$$\sum_{l=0}^{\infty}\sum_{m=-l}^{+l} Y_{lm}(\boldsymbol{n})Y^*_{lm}(\boldsymbol{n}') = \delta_\Omega(\boldsymbol{n},\boldsymbol{n}'), \tag{A2}$$

and we use the normalizations $Y^*_{lm}(\boldsymbol{n}) = (-1)^m Y_{l,-m}(\boldsymbol{n})$ and $Y_{00} = 1/\sqrt{4\pi}$. Isotropic spherical random fields can be expanded in Legendre polynomials or zonal harmonics, which constitute a complete orthogonal set over the interval $-1 \le x \le 1$, with the orthogonality and completeness relations

$$\int_{-1}^{+1} P_l(x)P_m(x)\mathrm{d}x = \frac{\delta_{lm}}{l+1/2}, \tag{A3}$$

$$\sum_{l=0}^{\infty}(l+1/2)P_l(x)P_l(x') = \delta(x-x'). \tag{A4}$$

A square-integrable function $f(x)$ on the interval $[-1, 1]$ admits the expansion

$$f(x) = \sum_{l=0}^{\infty} c_l P_l(x), \quad c_l = (l+1/2)\int_{-1}^{+1} f(x)P_l(x)\mathrm{d}x. \tag{A5}$$

If we put $x = \cos\theta = \boldsymbol{n}\boldsymbol{k}_0$, we find the Legendre expansion of the isotropic field $f(\boldsymbol{n}\boldsymbol{k}_0)$ on the sphere $|\boldsymbol{n}| = 1$ as

$$f(\boldsymbol{n}\boldsymbol{k}_0) = \frac{1}{4\pi}\sum_{l=0}^{\infty}(2l+1)C_l P_l(\boldsymbol{n}\boldsymbol{k}_0), \quad C_l = \int f(\boldsymbol{n}\boldsymbol{k}_0)P_l(\boldsymbol{n}\boldsymbol{k}_0)\mathrm{d}\Omega_{\boldsymbol{n}}. \tag{A6}$$

The multipole coefficients C_l are independent of the arbitrarily chosen unit vector $\boldsymbol{k}_0$. We also note $P_0(x) = 1$, $P_l(1) = 1$, as well as the reflection symmetry $P_l(x) = (-1)^l P_l(-x)$. This expansion can be traced back to spherical harmonics via the addition theorem (Newton 1982;

Jackson 1999)

$$P_l(\boldsymbol{k}_0\boldsymbol{n}) = \frac{4\pi}{2l+1}\sum_{m=-l}^{+l} Y_{lm}(\boldsymbol{k}_0)Y^*_{lm}(\boldsymbol{n}), \tag{A7}$$

where we may interchange $\boldsymbol{k}_0$ and $\boldsymbol{n}$. Combining equation (A7) with the completeness relation for spherical harmonics (A2), we find the Legendre series of the delta function on the unit sphere as stated in equation (2.13).

We consider isotropic spherical random fields (depending only on the polar angle θ), so that Legendre expansions of type (A6) in zonal harmonics $P_l(\cos\theta) = \sqrt{4\pi/(2l+1)}Y_{l0}(\boldsymbol{n})$ suffice. We note $\Delta_\Omega P_l(\cos\theta) = -l(l+1)P_l(\cos\theta)$, where Δ_Ω is the Laplace–Beltrami operator on the unit sphere (Landau & Lifshitz 1991). The high-l asymptotics

$$P_l(\cos\theta) \sim 2\frac{[1+\mathrm{O}(1/l)]}{\sqrt{2\pi l\sin\theta}}\cos\left(\left(l+\frac{1}{2}\right)\theta - \frac{\pi}{4}\right) \tag{A8}$$

can be used to identify the wavelength $\lambda \sim 2\pi/(l+1/2) \sim 2\pi/\sqrt{l(l+1)}$ on the unit sphere (Jeans 1923). This gives an estimate of the angular resolution achieved by high-order multipole moments in the Legendre expansion (2.27) of the two-point function $\langle T(\boldsymbol{p})T(\boldsymbol{p}')\rangle$, where we put $\boldsymbol{p}_0\boldsymbol{p}'_0 = \cos\theta$.

APPENDIX B: EULER PARAMETRIZATION OF HERMITIAN SPECTRAL MATRICES

We consider a positive semidefinite Hermitian 3×3 matrix g_{mn}, cf. (3.1), which we decompose as

$$g_{mn} = R_3^{-1}R_2^{-1}R_1^{-1}\mathrm{diag}[a_1,a_2,a_3]R_1R_2R_3, \tag{B1}$$

with real diagonal coefficients $a_j \geq 0$, analogous to the two-dimensional case in equations (3.3) and (3.4). Positive definiteness requires $a_j > 0$. The matrices $R_i(\theta_i,\psi_i,\chi_i)$, $i=1,2,3$, in equation (B1) denote SU(3) subgroups composed of the SU(2) matrices

$$U_i(\theta_i,\psi_i,\chi_i) = \begin{pmatrix} \mathrm{e}^{\mathrm{i}\psi_i}\cos\theta_i & \mathrm{e}^{\mathrm{i}\chi_i}\sin\theta_i \\ -\mathrm{e}^{-\mathrm{i}\chi_i}\sin\theta_i & \mathrm{e}^{-\mathrm{i}\psi_i}\cos\theta_i \end{pmatrix},$$
$$U_i^{-1}(\theta_i,\psi_i,\chi_i) = U_i(-\theta_i,-\psi_i,\chi_i) \tag{B2}$$

in the following way:

$$R_1(\theta_1,\psi_1,\chi_1) = \begin{pmatrix} 1 & 0 & 0 \\ 0 & \mathrm{e}^{\mathrm{i}\psi_1}\cos\theta_1 & \mathrm{e}^{\mathrm{i}\chi_1}\sin\theta_1 \\ 0 & -\mathrm{e}^{-\mathrm{i}\chi_1}\sin\theta_1 & \mathrm{e}^{-\mathrm{i}\psi_1}\cos\theta_1 \end{pmatrix} = \begin{pmatrix} 1 & 0 \\ 0 & U_1 \end{pmatrix},$$
$$R_2(\theta_2,\psi_2,\chi_2) = \begin{pmatrix} \mathrm{e}^{\mathrm{i}\psi_2}\cos\theta_2 & 0 & \mathrm{e}^{\mathrm{i}\chi_2}\sin\theta_2 \\ 0 & 1 & 0 \\ -\mathrm{e}^{-\mathrm{i}\chi_2}\sin\theta_2 & 0 & \mathrm{e}^{-\mathrm{i}\psi_2}\cos\theta_2 \end{pmatrix},$$
$$R_3(\theta_3,\psi_3,\chi_3) = \begin{pmatrix} \mathrm{e}^{\mathrm{i}\psi_3}\cos\theta_3 & \mathrm{e}^{\mathrm{i}\chi_3}\sin\theta_3 & 0 \\ -\mathrm{e}^{-\mathrm{i}\chi_3}\sin\theta_3 & \mathrm{e}^{-\mathrm{i}\psi_3}\cos\theta_3 & 0 \\ 0 & 0 & 1 \end{pmatrix} = \begin{pmatrix} U_3 & 0 \\ 0 & 1 \end{pmatrix}. \tag{B3}$$

The inverse matrices in the decomposition (B1) are found as

$$R_i^{-1}(\theta_i,\psi_i,\chi_i) = R_i(-\theta_i,-\psi_i,\chi_i). \tag{B4}$$

If we put $\psi_i = \chi_i = 0$, $i=1,2,3$, then the product $R_1(\theta_1)R_2(-\theta_2)R_3(\theta_3)$ is a classical Euler parametrization of the rotation group SO(3), with $0 \leq \theta_{1,3} < 2\pi$ and $0 \leq \theta_2 \leq \pi$. In this case, the Hermitian g_{mn} in equation (B1) is real and symmetric. Here, we do not impose any restrictions on the angles θ_i, χ_i and ψ_i other than reality.

In N dimensions, the Euler parametrization of a Hermitian matrix g_{mn}, $m,n = 0,\ldots,N-1$, is performed in like manner,

$$g_{mn} = R_{N(N-1)/2}^{-1}\cdots R_1^{-1}\mathrm{diag}[a_1,\ldots,a_N]R_1\cdots R_{N(N-1)/2}, \tag{B5}$$

with $\binom{N}{2}$ three-parameter subgroups $R_i(\theta_i,\psi_i,\chi_i)$, $i=1,\ldots,N(N-1)/2$, of SU(N), each of them defined by an SU(2) matrix inserted into an $N\times N$ identity matrix according to the pattern (B3). In this way, the matrices g_{mn} are parametrized by N^2 independent real parameters, $(a_j \geq 0, \theta_i, \varphi_i)$, $j=1,\ldots,N$ and $i=1,\ldots,N(N-1)/2$, where φ_i can be chosen as linear combinations of the $N(N-1)$ angles ψ_i and χ_i of the SU(N) subgroups $R_i(\theta_i,\psi_i,\chi_i)$. For the amplitudes and angles, we use a spectral parametrization $(a_j(k), \theta_i(k), \varphi_i(k))$ analogous to equations (3.15) and (3.16), that is, a linear or quadratic k dependence of the angles, and Gaussian power-law densities as amplitudes.

This paper has been typeset from a TEX/LATEX file prepared by the author.